Multi-centennial climate change in a warming world beyond 2100

Sun-Seon Lee[1,2*], Sahil Sharma[1,2], Nan Rosenbloom[3], Keith B. Rodgers[4*], Ji-Eun Kim[1,2], Eun Young Kwon[1,2], Christian L.E. Franzke[1,2], In-Won Kim[1,2], Mohanan Geethalekshmi Sreeush[5], and Karl Stein[1,2]

[1]Center for Climate Physics, Institute for Basic Science, Busan, Republic of Korea
[2]Pusan National University, Busan, Republic of Korea
[3]National Center for Atmospheric Research, Boulder, CO, USA
[4]WPI-Advanced Institute for Marine Ecosystem Change, Tohoku University, Sendai, Japan
[5]Alfred Wegener Institute, Helmholtz Centre for Polar and Marine Research, Am Handelshafen 12, 27570 Bremerhaven, Germany

Correspondence to: Sun-Seon Lee (sunseonlee@pusan.ac.kr) and Keith B. Rodgers (keith.rodgers.b2@tohoku.ac.jp)

Abstract. Sustained anthropogenic perturbations are anticipated to influence Earth's climate system well beyond the 21st century. Despite growing interest in climate change after 2100 and improved computational resources, multi-century climate projections remain limited in number. Here, we examine a set of 10 ensemble simulations extending the Community Earth System Model 2 large ensemble (CESM2-LE) from 2101 to 2500 under the shared socio-economic pathway (SSP)3-7.0 scenario, which involves the reduction of fossil and industrial CO_2 emissions to zero by 2250. By the year 2500, substantial forced changes are projected in both the spatial and temporal characteristics of variability and mean states. Post-2100, El Niño-Southern Oscillation variability is expected to diminish, while the tropical intraseasonal variability will notably strengthen. The mean state changes include a global mean temperature rise of 12 °C and a 23.5 % increase in global precipitation compared with historical observations. Additionally, substantial soil carbon release from permafrost thawing is projected over Siberia and Canada, resulting in a shift of land from a carbon sink to a carbon source after the 22nd century. The ocean experiences a rapidly diminished capacity to absorb anthropogenic CO_2 after the 21st century, while nevertheless continuing to act as a carbon sink, with an increased contribution from the Southern Ocean to total carbon uptake. The model also projects a considerable decline in low-latitude marine primary production, which is linked to a considerable depletion of PO_4 in the local mesopelagic domain. At urban scales, the extended simulations reveal substantial projected changes in the amplitude and phasing of precipitation seasonality, with the same holding for the partial pressure of CO_2 in seawater at regional scales, demonstrating that post-2100 changes are not simply amplifications of projected 21st century changes. Taken together, these new simulations highlight the far-reaching impacts of multi-centennial climate change on both human societies and global ecosystems.

1. Introduction

To date, the scientific literature on climate change projections has primarily focused on projecting changes to the year 2100 (e.g., IPCC, 2021), motivated by the need to guide policy and societal decisions that affect multiple human generations. However, several critical components of the climate system such as heat and carbon reservoirs will respond slowly over timescales of multiple centuries, and their response times will play a strong role in determining the impact of the long-term climate change (Oh et al., 2024; Armour et al., 2016; Koven et al., 2022; Schuur et al., 2015; Cheng et al., 2019). Therefore, given that the legacy of human-induced perturbations will persist well beyond 2100, particularly through the multi-century to multi-millennia residence time of CO_2 in the atmosphere (Archer et al., 2009), protocols have been developed to extend Coupled Model Intercomparison Project (CMIP) simulations to 2500 (Meinshausen et al., 2020). The growing interest in these extended timescales can be seen in the increasing number of studies that consider multi-century projections of climate change (e.g., Randerson et al., 2015; Moore et al., 2018; Koven et al., 2022; Hezel et al., 2014; Mahowald et al., 2017; Wang et al., 2024; Peng et al., 2024; Geng et al., 2024). Under relatively strong emissions scenarios, these studies emphasize that the adverse impacts of climate change are expected to persist well beyond 2100. As an example, an inter-model comparison of

global carbon cycle simulations identified general consistencies in the sign of mean state responses to strong anthropogenic forcing, focusing on carbon uptake by the ocean and terrestrial systems that has potential impacts for climate feedbacks (Koven et al., 2022). In the models, the uptake of carbon by the ocean gradually declines, but remains positive throughout the 22nd and 23rd centuries. Terrestrial carbon cycle tends to shift from a net sink to either a neutral state or a net source.

45 Given the expected importance of ocean overturning structures in sustaining marine ecosystems (Sarmiento et al., 2004), it is also essential to examine how marine ecosystems may be impacted over longer timescales. This was first considered for the case of an extension simulation with an Earth system model to 2300 by Moore et al. (2018). Under historical and extended Representative Concentration Pathway (RCP) 8.5 forcing to 2300 with the Community Earth System Model 1 (CESM1), the study reported a 24 % decrease in primary production and a 41 % decrease in the carbon export across the 100 m horizon in

50 the low latitudes (30°S-30°N) to 2300. This decrease was argued to be due to an enhanced nutrient retention in the Southern Ocean due to a poleward shifting of westerlies and sea ice melt, which then in turn led to a reduction in the supply of nutrients to the low latitudes by a Subantarctic Mode Water conduit. The interpretative framework of Moore et al. (2018) built on the long-standing paradigm for Southern Ocean dominance of low-latitude productivity originally considered for the mean state by Sarmiento et al. (2004).

55 Subsequently, Rodgers et al. (2024) revisited the question of future changes in low-latitude primary production and export using five distinct CMIP phase 6 (CMIP6) models, arguing instead for the critical role of low-latitude remineralization and water mass renewal in determining the response to sustained warming over multiple centuries. They underscored the pivotal role of the transfer efficiency of the ocean's twilight or mesopelagic zone, defined as the ratio of the export flux at the base of the mesopelagic domain to the export flux at the base of the euphotic zone, in elucidating the transient responses of Earth

60 system in the deep future. Although they established that thermocline retention of nutrients serves as a first-order control on future projections, emphasizing the central importance of temperature-dependent remineralization, they did not address the degree to which this might be modulated by the stoichiometric plasticity mechanism proposed by Kwon et al. (2022) and Tanioka et al. (2022), both of which had evaluated simulations spanning from 1850 to 2100.

In the context of forced changes in variance within the Earth system, recent studies have explored the sustained anthropogenic

65 impacts on the variability of the El Niño-Southern Oscillation (ENSO), arguing for a reduction in ENSO variability under strong forcing beyond 2100 (Peng et al., 2024; Geng et al., 2024). In addition, a recent study presented the possibility of a permanent El Niño with reduced ENSO amplitude in a high-CO_2 world, but that study also pointed out that unforced variability at the centennial scale for this case is comparable to the projected changes under a wide range of CO_2 forcing (Callahan et al., 2021). Future ENSO projections including changes in amplitude, frequency, phase-locking, and skewness, particularly the

70 post-2100 ENSO changes remain highly uncertain. For this reason, further investigation into future ENSO changes in longer-term timescales is needed. One related recent finding is that the Indian Ocean Dipole variability, which interacts with ENSO, is projected to increase in the eastern pole in the 21st century, followed by a reduction thereafter (Wang et al., 2024). These findings indicate that forced changes in Earth system variability may exhibit non-linear responses to sustained greenhouse warming after 2100. Consequently, to inform long-term adaptation planning and decision-making, it is of great value to have

75 multi-century projections derived from an ensemble of simulations with a single model, which can provide insights into potential risks associated with ongoing greenhouse warming.

For this study, we have chosen to investigate forced changes in the climate system out to the year 2500 by extending 10 members of the 100-member Community Earth System Model 2 large ensemble (CESM2-LE; Rodgers et al., 2021) from 2101 to 2500. This is done by leveraging an extension of the shared socio-economic pathway (SSP)3-7.0 scenario applied to the

80 CESM2-LE. The choice of not only an ensemble of simulations, but also the application of CESM2, offers several advantages

for understanding future changes beyond 2100. An ensemble provides a more robust characterization of forced changes in the mean state and variability (Deser et al., 2020). In addition, advances in soil biogeochemistry representation with vertical resolution in Community Land Model Version 5 (CLM5; Lawrence et al., 2019) enhance the study of how permafrost thaw could impact the soil carbon reservoir in high latitudes of the Northern Hemisphere after the 21st century.

85 ## 2. Extension of 10 members of CESM2-LE to 2500

Here, we present a 10-member extension of the CESM2-LE to the year 2500. The original CESM2-LE employs historical (1850-2014) and projected (2015-2100) SSP3-7.0 forcing fields (O'Neill et al., 2016) with the latter representing a medium-high reference scenario within the "regional rivalry" socio-economic family (Meinshausen et al., 2020). All CESM2-LE simulations have nominal 1° x 1° spatial resolution. The selected 10 members from the CESM2-LE for extension are the
90 macro-perturbation simulations which were initialized from 10 model states ranging from year 1011 to 1191 (20-year intervals) of a pre-industrial control simulation conducted with CESM2 (Danabasoglu et al., 2020). For a fuller description of CESM2-LE, the reader is referred to Rodgers et al. (2021).

A detailed description of the underlying model components of CESM2 can be found in Danabasoglu et al. (2020). For the purposes of this study, we first summarize the model components before describing the forcing and boundary conditions used
95 in the extended simulations. The atmospheric model component is the Community Atmosphere Model version 6 (CAM6; Danabasoglu et al., 2020), and thus is distinct in the model components from the single ensemble member of CESM2-WACCM simulation to 2300 under SSP5-8.5 presented by Koven et al. (2022). The land model consists of the CLM5 (Lawrence et al., 2019). The physical ocean and sea ice components are the Parallel Ocean Program version 2 (POP2; Smith et al., 2010) and the CICE Version 5.1.2 (CICE5; Bailey et al., 2020), respectively. CESM2 uses the Marine Biogeochemistry Library (MARBL; Long et al., 2021) for ocean ecosystem modeling. In the context of interpreting the sustained strong ocean warming
100 on biogeochemical and ecosystem impacts, it is important to note that MARBL does not account for the effect of ocean warming on remineralization rates. As noted by Rodgers et al. (2024), this may have important implications for projected future concentrations of mesopelagic and thermocline nutrients, and consequently for primary production and export.

In the extension of the CESM2-LE from 2101 to 2500, fossil and industrial CO_2 emissions are effectively ramped down to
105 zero by 2250 under the extended SSP3-7.0 protocol, as shown in Fig. 1a (Meinshausen et al., 2020). Figure 1b presents the time evolution of global mean greenhouse gas mixing ratios (CO_2, CH_4, N_2O, and CFCs) used in these simulations. The global mean atmospheric CO_2 mixing ratio at the end of the 25th century under the SSP3-7.0 scenario is approximately 1371 ppm. Even though fossil and industrial CO_2 emissions decrease after the year 2100 and are ramped down to zero by 2250 in the simulations, the atmospheric CO_2 concentration peaks around the year 2240 (at approximately 1515 ppm) and declines
110 modestly thereafter. The top-of-the-atmosphere radiation imbalance exhibits a strong increase throughout the 21st century, peaking at approximately 3.5 W m^{-2} in the mid-22nd century, and then gradually decreasing to approximately 1.6 W m^{-2} by the year 2500 (Fig. 1c). Under the SSP3-7.0 forcing, global mean surface air temperature perturbations exceed 12 °C at the end of 25th century relative to the 1850-2019 period, i.e., the HadCRUT4 (Morice et al., 2012) observation period (Fig. 1d). If the 1850-1900 baseline is used, the global mean surface air temperature change closely matches the change observed with the
115 1850-2019 baseline.

Additionally, SSP3-7.0 is characterized by relatively strong land use changes, particularly a global reduction in forest cover by 2100, along with high emissions of near-term climate forcers including tropospheric aerosols, tropospheric O_3 precursors, and CH_4 (O'Neill et al., 2016). Among the SSP extension scenarios, SSP3-7.0 is the scenario with the highest atmospheric mixing ratios for both CH_4 and N_2O (Meinshausen et al., 2020). All other forcings, including aerosols and land use, were fixed

120   at the values of the year 2100 in the extended simulations. This study uses 10 ensemble simulations from both CESM2-LE
       and extended simulations covering the entire period from 1850 to 2500 (651 years).

       We also incorporated output from the RAD simulation, known as radiatively coupled in CMIP terms, to understand carbon
       cycle perturbations. In the RAD simulations, a constant pre-industrial CO_2 mixing ratio is maintained for biogeochemical
       fluxes of CO_2 over land and ocean, e.g., air-sea gas exchange, while the change in atmospheric CO_2 affects the radiation
125   balance of the atmosphere only.
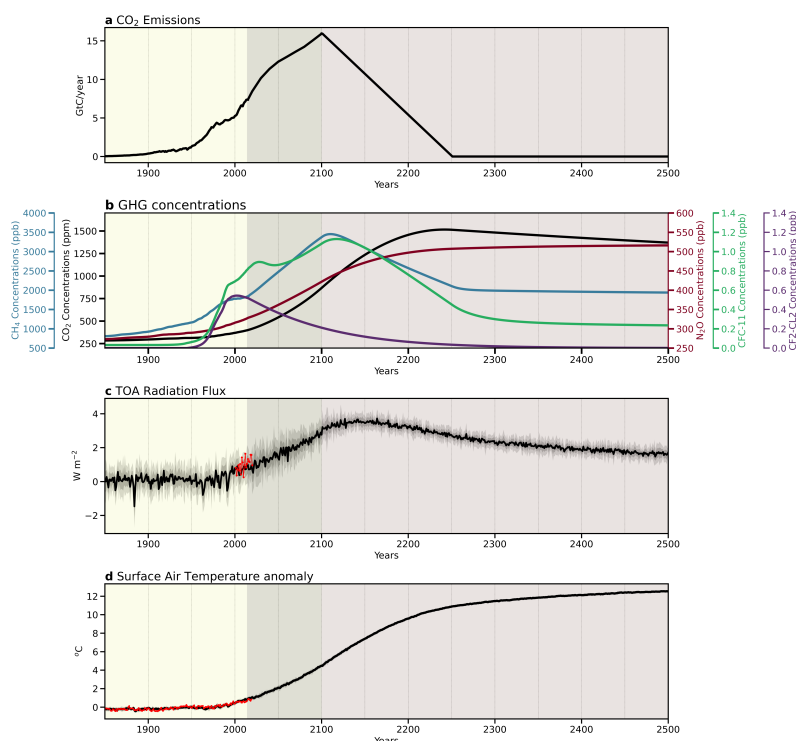
Figure 1: Time series of global mean (a) fossil fuel and industrial CO_2 emissions and (b) greenhouse gas concentrations over 1850-2500 for the CESM2-LE extension simulations. Values are taken from Meinshausen et al. (2020). Time series of global fields over 1850-2500 for 10 ensemble members for (c) top-of-atmosphere radiative imbalance (W m^{-2}) along with the CERES-EBAF product
130   **(Loeb et al., 2018; Loeb et al., 2009) and (d) anomalies of global mean surface air temperature (°C) along with HadCRUT4 (Morice et al., 2012). In (c) and (d), anomalies are calculated with respect to the period spanned by the observations.**

3. Results

3.1 Multi-centennial changes in mean state and variability

       To provide a perspective on the overall long-term climate changes, in addition to the changes in the top-of-the-atmosphere
135   radiation imbalance and temperature (Fig. 1c, d), we begin by presenting the evolution of mean state for several key variables
       over the time interval from 1850 to 2500 (Fig. 2). The anomalies shown in Fig. 2 were calculated relative to the observation
       period for each case that includes an observational dataset, following the procedure used in the CESM2-LE overview study
       (Rodgers et al., 2021). The global mean precipitation anomalies show gradual increases from the 21st century to the end of the
       25th century, with a 23.5 % increase in global mean precipitation over the 2401-2500 period relative to the 1979-2020 satellite
140   observational period (Fig. 2a). Overall, annual mean precipitation increases are evident across all latitudinal bands except for
       45°S-15°S and 15°N-40°N (Fig. S1a-f).

Ocean heat accumulation, as indicated by changes in ocean heat content, provides a measure of the excess anthropogenic heat stored in the ocean (Garcia-Soto et al., 2021), and complements global mean surface temperature changes. The observed changes indicate that global ocean heat content in the upper 2,000 m increases by 351.4 ± 59.8 ZJ from 1958 to 2019 (Cheng et al., 2022). Our simulations also show a consistent global ocean warming in the upper 2,000 m throughout the entire simulation period (Fig. 2b). By the end of the 25th century, the projections indicate a cumulative increase of ~17,000 ZJ, which is approximately seven times higher than the projected heat content perturbation by the end of the 21st century in the CESM2-LE (Rodgers et al., 2021). A rapid growth in ocean heat content leads to considerable changes in sea ice melting, exerting a large influence on the global heat balance. In contrast to the stabilized Arctic sea ice extent projected by around 2040 under the low-emission SSP1-2.6 scenario of CMIP6 (Davy and Outten, 2020), our simulations project a continuous decline of Arctic sea ice from the late 20th century to the mid-22nd century, followed by an ice-free condition thereafter (Fig. 2c) and similar trend pattern is seen in the Southern Ocean sea ice as well. The loss of sea ice and resultant environmental changes at a local scale have already influenced weather and climate outside of the Arctic and Antarctic regions (e.g., Screen et al., 2018). Given the crucial role of the Atlantic Meridional Overturning Circulation (AMOC) in distributing heat within the Earth's climate system, a number of previous studies have evaluated projected AMOC changes (e.g., Ditlevsen and Ditlevsen, 2023; Weijer et al., 2020; Liu et al.; Roberts et al., 2020). As shown in many climate model simulations including CESM2-LE (e.g., Rodgers et al., 2021; Weijer et al., 2020), our extended simulations project a slowing of the AMOC in response to anthropogenic warming until the late 22nd century, with a slight recovery following the minimum state of the AMOC strength (Fig. 2d).

The response of net primary productivity (NPP) in the terrestrial biosphere and the ocean to anthropogenic forcing is an indicator of changes in the rate at which carbon is fixed at the base of respective food webs over the land and ocean, with implications for global ecosystems. While marine NPP shows a relatively modest decrease after the end of the 21st century, terrestrial NPP exhibits a considerable increase from the end of the 20th century to the mid-22nd century and it saturates thereafter (Fig. 2e). The fact that changes are much larger in terrestrial NPP than in marine NPP is due to terrestrial NPP being strongly modulated by changing atmospheric CO_2 concentrations through CO_2 fertilization effects (e.g., Prentice et al., 2001). Our extended simulations suggest that the globally integrated ocean NPP declines by 12 % from 48 PgC yr^{-1} in 1850 to 42 PgC yr^{-1} in 2500. As we will see in Figs. 9-11, future low-latitude decreases in marine NPP are accompanied by large decreases in PO_4 and NO_3 throughout the ocean's mesopelagic domain (100 m to 1000 m depth), with this having a deleterious impact on the rate at which macronutrients become available within the euphotic zone through overturning structures. The uptake rates of CO_2 by global land and ocean increase as anthropogenic CO_2 emissions increase until the end of the 21st century (Fig. 2f). However, after the end of the 21st century, the uptake rates of both land and ocean decrease, indicating reductions in net terrestrial and oceanic carbon sinks. The substantial decline in oceanic carbon uptake, with positive values indicating a flux into the ocean, can be described as a weakened solubility pump through a reduced CO_2 buffering capacity of seawater, as well as through a reduction in the soft tissue component of the biological pump and a strong reduction in AMOC overturning (e.g., Chikamoto and DiNezio, 2021). Nevertheless, our simulations indicate that global ocean persists as a weakened carbon sink until the year 2500. The decrease in net carbon uptake rate of the terrestrial system after the end of the 21st century is largely attributed to an increase in microbial carbon decomposition and the release of carbon in regions impacted by permafrost thawing. In our simulations, the permafrost regions, defined as areas where the active layer thickness of soils is less than 3 m, begin to decline at the end of the 20th century, followed by a continued reduction until the mid-22nd century (Fig. 2g). Future changes in terrestrial and marine biogeochemistry, as well as potential climate-carbon feedbacks, will be discussed further in Section 3.3.

Our simulations demonstrate increases in greenhouse warming-driven stability in both the atmosphere and the ocean over global scales. A positive anomaly in atmospheric stability from the early 21st century onwards indicates increased stabilization of the atmosphere relative to its present-day climate conditions (Fig. 2h). The upper tropospheric amplification, i.e., enhanced

warming of the upper troposphere relative to the surface (e.g., Santer et al., 2017), is responsible for this increased stability of
185   the atmosphere. Also, an increase in the ocean's surface temperature due to greenhouse warming leads to an enhanced upper
ocean stratification, as measured by the density differences between the 300 m and 50 m depths. The stronger upper ocean
stratification is associated with a decrease in the mixed layer depth (Fig. 2i,j).
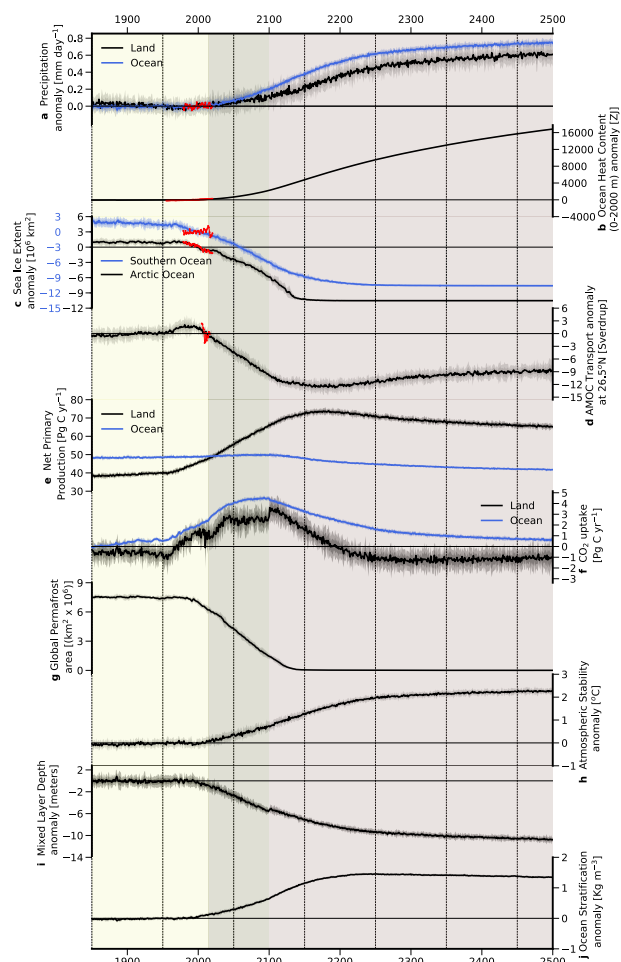
190   **Figure 2: Time series of global fields over 1850-2500 for 10 ensemble members. (a) Anomalies of the precipitation (mm day⁻¹) over the land (black) and over the ocean (blue) along with the Global Precipitation Climatology Project (GPCP) (Adler et al., 2012; Adler et al., 2003), (b) anomalies of ocean heat content integrated over the upper 2000 m (ZJ) along with an observation-based product (Ishii et al., 2017), (c) anomalies of sea ice extent (10⁶ km²) for the Arctic (black) and Southern Ocean (blue), with observed sea ice extent over 1979-2020 (Fetterer, 2017), (d) Atlantic Meridional Overturning Circulation (AMOC) transport anomalies at 26.5°N**
195   **(Sv), with RAPID array observations (Frajka-Williams et al., 2019), (e) globally integrated net primary productivity (NPP) (Pg C yr⁻¹) over the land (black) and over the ocean (blue), (f) globally integrated net CO₂ uptake (Pg C yr⁻¹) over the land (black) and over the ocean (blue), (g) global permafrost area defined as the active layer thickness is less than 3 m (km² x 10⁶), (h) globally averaged atmospheric stability anomaly (difference between 200 hPa air temperature and surface air temperature) (°C) relative to 1850-1949 period, (i) anomalies of mixed layer depth (m) relative to 1850-1949 period, and (j) ocean stratification anomaly**
200   **(difference between potential density at 300 m and 50 m) (kg m⁻³) relative to 1850-1949 period. For model fields, bold lines represent ensemble means, and dark and light shading represent 1 standard deviation (SD) and 2 SD variability. For each case, where observational products (red) are included, anomalies are calculated with respect to the period spanned by the observations. For comparison with the 100-member CESM2-LE over 1850-2100, the reader is referred to Fig. 1 of Rodgers et al. (2021), where a subset of the variables shown here are presented.**

205

Figure 3 displays the spatial distributions of climatologies over the 1850-1949 period and projected future changes for several
key fields. Here, we consider the periods 2150-2249 and 2401-2500 as the 'extended future' and the 'deep future' periods,

respectively. With a global mean warming level greater than 12 °C by the end of the 25th century relative to the 1850-2019 observation period (Fig. 1d), more pronounced warming over land is projected for the extended future period, and the warming

210 is then intensified in the deep future (Fig. 3a-c). The strongest warming, exceeding 28 °C, is found over Nunavut, Canada. High-latitude regions are projected to warm more substantially than low-latitude regions (Fig. 3c), except for the central and eastern equatorial Pacific, implying the continuation of polar amplification (e.g., Koven et al., 2022) and thereby as a consequence a weakened equator-to-pole surface temperature gradient beyond 2100, in particular over the Northern Hemisphere. Regarding the tropical Pacific mean state changes, most climate models show a reduction in their zonal sea

215 surface temperature (SST) gradient due to preferentially stronger eastern relative to western equatorial Pacific warming under increased CO_2 concentrations (e.g., Vecchi and Soden, 2007; Fredriksen et al., 2020). By the 25th century, the eastern equatorial Pacific shows an enhanced warming of 8-10 °C relative to the 1850-1949 period, leading to a further weakening of the west-east SST gradient beyond 2100. This change affects ocean-atmosphere interactions encompassing the Pacific Walker circulation (e.g., Chung et al., 2019; Zhang and Karnauskas, 2017), tropical precipitation structure (e.g., Chadwick et al., 2013),

220 ENSO variability (e.g., Cai et al., 2021; Fredriksen et al., 2020; Peng et al., 2024), and ultimately global ecosystems (Lee et al., 2022).

The spatial distribution of precipitation changes for the 25th century relative to the historical period is similar to the pattern of changes by the end of the 21st century shown in Rodgers et al. (2021). However, the magnitude of perturbations is substantially larger (Fig. 3f). One notable feature of the tropical precipitation changes is the disappearance of the South Pacific Convergence

225 Zone (SPCZ), which is characterized by a northward shift with loss of its diagonal orientation towards the subtropics (Fig. S2b, c). The equatorward movement and the projected change in the zonal structure of the SPCZ in the future can be linked to the SST response in the central equatorial Pacific (Cai et al., 2012). Meanwhile, the weakening of the AMOC (Fig. 2d) is related to the southward shift of Intertropical Convergence Zone (ITCZ) (Vellinga and Wood, 2002; Bellomo et al., 2021), leading to increases in equatorial precipitation (Fig. 3e, f). These changes in tropical precipitation structures result in the

230 merging of the precipitation bands associated with the ITCZ and the SPCZ. Consequently, the tropical precipitation zone becomes narrower and areas that are typically dry between the two tropical convergence zones experience wet conditions in the future (Fig. S2a-c). The increased precipitation along the equatorial Pacific is accompanied by greater upward atmospheric motion in this region (Fig. 3h, i and Fig. S2e, f). More broadly, the enhanced anomalous upward motion is accompanied by weakened easterlies occur over the tropical Pacific Ocean (Fig. 3k, l), which is likely linked to the changes in the east-west

235 SST gradient (Fig. 3c), suggesting a weakening of the Pacific Walker circulation due to greenhouse warming. In addition to the weakening of the easterlies in the equatorial Pacific, our simulations project a substantial reduction of the trade winds in the extended future, with this change becoming more pronounced in the deep future (Fig. 3k, l). In contrast to the changes in the tropics, westerly winds in the Southern Hemisphere show an intensification poleward of 50°S with a reduction equatorward of 50°S (Fig. 3l), consistent with a poleward shift of westerlies found in previous studies (e.g., Deng et al., 2022).

240
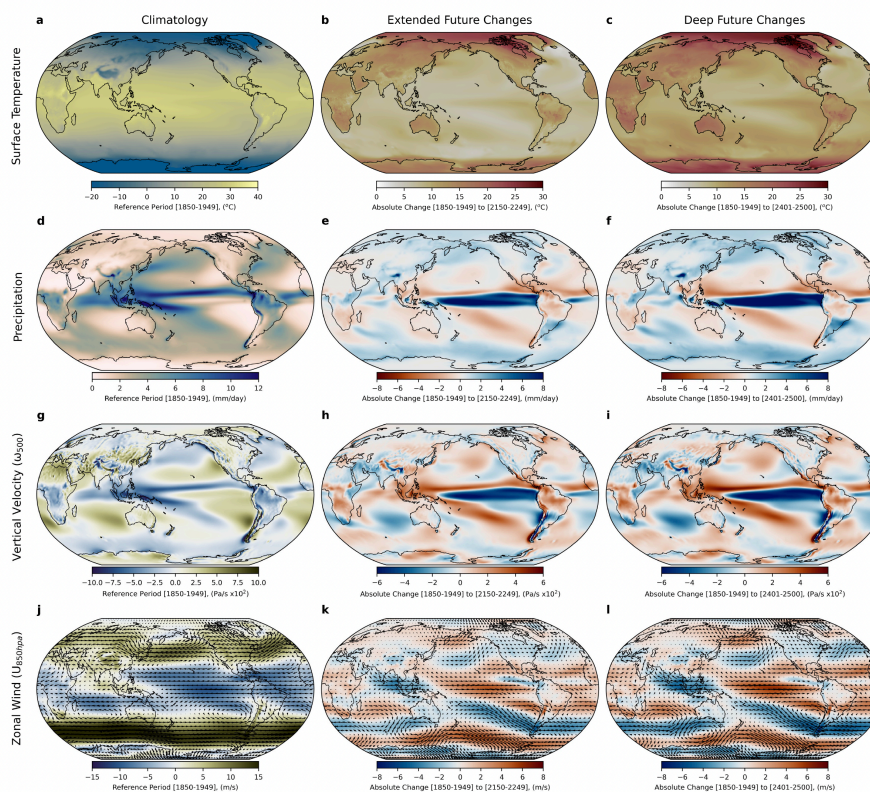
Figure 3: Climatology (period 1850-1949) (first column) and future perturbations over the period 2150-2249 (second column) and over the period 2401-2500 (third column) relative to 1850-1949. (a-c) Surface temperature (°C), (d-f) precipitation (mm day^{-1}), (g-i) 500 hPa vertical p-velocity (Pa s^{-1} x 10^2), and (j-l) 850 hPa wind (vector, m s^{-1}) and its zonal component (shading, m s^{-1}).

245

In addition to examining spatial patterns of mean state changes, we also investigated changes in the spatial pattern of surface temperature and precipitation variability (Fig. 4). Except for Africa, south/southeast Asia, Australia, South America, and the North Atlantic regions, the inter-ensemble spread in surface air temperature is projected to decrease, especially over high-latitude land regions in the Northern Hemisphere (Fig. 4b, c), indicating strong forced changes in variance over these regions.

250 Similarly, suppressed temperature variability is projected over the equatorial Pacific, suggesting a reduction in ENSO variability. The variability of ENSO, calculated by the 30-year running standard deviations of monthly Niño3.4 SST, exhibits a substantial reduction beyond the 21st century (Fig. 4d), which is consistent with previous studies (Peng et al., 2024; Geng et al., 2024). These studies suggest that reduced ENSO variability is linked to a weakened thermocline feedback due to collapsed equatorial ocean upwelling and the spread of convection to the eastern equatorial Pacific. Unlike with surface temperature, the

255 dominant change in future precipitation variability consists of an increase over most regions, with the exception of the tropical zone within the latitude bands spanning approximately 5°N-25°N and 35°S-10°S, where a decline in the mean precipitation is projected. As a consequence of the merged tropical precipitation bands through the disappearance of the SPCZ (Fig. 3e, f), precipitation variability along the equator in the Pacific increases strongly by the deep future period (Fig. 4g). Precipitation variability in the Niño3.4 region shows a peak in the mid-21st century along with ENSO SST variability, but there is a rebound

260 in the mid-23rd century (Fig. 4h).
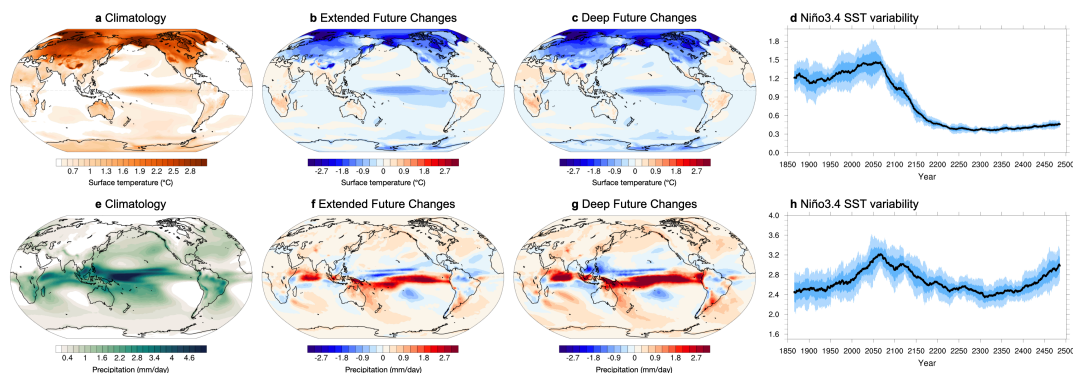
Figure 4: Time-averaged across-ensemble standard deviation of the boreal winter (DJF) mean (a) surface temperature (°C) and (e)
265 **precipitation (mm day⁻¹) over the period 1850-1949. Future changes of the standard deviation values of (b, c) surface temperature**
and (f, g) precipitation over the period 2150-2249 and over the period 2401-2500, respectively, relative to 1850-1949. (d, h) 30-year
running standard deviations of monthly Niño3.4 SST and precipitation, respectively.

Furthermore, we explored future changes in the Madden-Julian Oscillation (MJO), the dominant mode of tropical intraseasonal
270 variability during boreal winter (Madden and Julian, 1972). Due to minor adjustments to the deep convection scheme, and the
inclusion of the unified turbulence scheme, MJO representation in CESM2 has improved relative to CESM1 (Danabasoglu et
al., 2020). As a result, the MJO's eastward movement from the Western Indian Ocean into the central Pacific is represented in
CESM2 (Danabasoglu et al., 2020). Here, overall MJO activity is assessed through a wavenumber-frequency diagram
(Wheeler and Kiladis, 1999; Waliser et al., 2009) with 10°S-10°N averaged daily precipitation and 850 hPa zonal wind for the
275 historical and future periods (Fig. 5). During the historical period, for both precipitation and 850 hPa zonal wind, maximum
power is observed in the 30-80 day period and wavenumber 1-2, with greater eastward than westward power (Waliser et al.,
2009). In the extended and deep future periods, the spectral amplitude in the intraseasonal frequency domain is projected to
increase markedly, indicating the strengthening of the MJO intensity in response to greenhouse warming (Figs. 5b, c, e and f).
Furthermore, the maximum variance of both precipitation and 850 hPa zonal wind is projected to shift towards higher
280 frequencies, with the maximum occurring at periods shorter than 30 days, closer to 25 days (Cui and Li, 2019). In particular,
it is projected that the amplitude of power spectrum for precipitation in the extended and deep future periods will be
approximately ten times greater than those observed in the historical period (Fig. 5c). Thus, in these extended simulations, we
identify a remarkable future transition from a case where ENSO variability is dominant in the equatorial region to a state where
it is greatly diminished and the MJO becomes more prominent. This will have a number of implications for local ecosystems
285 and biogeochemical cycling in the tropics, as well as for teleconnections away from the regions impacted directly.
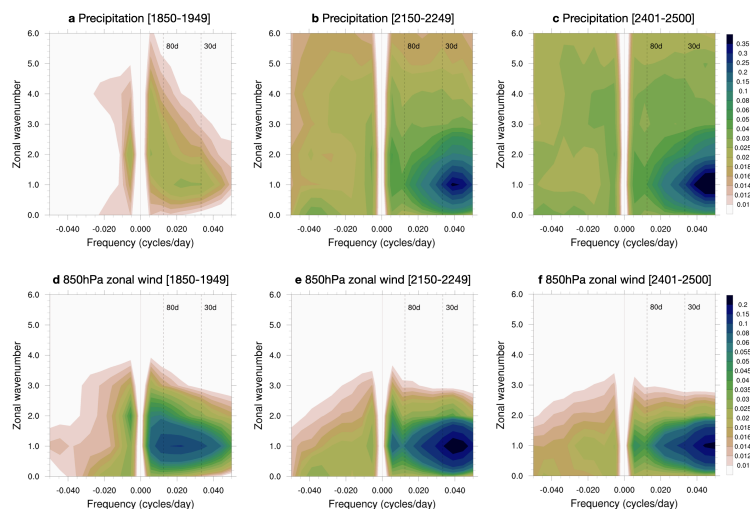
Figure 5: Wavenumber-frequency power spectra for 10°S-10°N averaged precipitation (mm² day-²; upper panels) and 850 hPa zonal wind (m² s⁻²; lower panels) for November-April. (a, d) Period 1850-1949, (b, e) period 2150-2249, and (c, f) period 2401-2500. The spectra are calculated for individual ensemble members and then averaged across the 10 ensemble members.

3.2 Changes in seasonality

As described in the previous section, sustained multi-century warming trends will alter the spatial and temporal characteristics of mean precipitation. Additionally, changes in the seasonal phasing and the magnitude of precipitation at a regional scale will drive substantial hydrological changes along with impacts on the water resources. For instance, when averaged over the tropical band between 15°S and 15°N, the seasonal cycle of precipitation in the 24th and 25th centuries is projected to have two peaks, occurring in May and August, instead of the single peak that is typically observed from mid-June to mid-July over the historical period (Fig. S1c, i). Furthermore, mean state changes are expected to lead to shifts in frequency, intensity, and duration of precipitation extremes at the local scale (Sun et al., 2022), potentially resulting in substantial social and economic losses. Figure S1 indicates that day-to-day variations in spatially averaged precipitation tend to increase along with the increases in time mean averages. This is especially evident to the north of 40°N and south of 45°S during rainy seasons, implicating future increases in the magnitude and frequency of extreme precipitation over those regions. Therefore, a better understanding of the signature of forced changes at the regional or local scales can provide valuable insights into how strong anthropogenic forcing will impact extreme precipitation events and water availability.

Figure 6 shows the distributions of the seasonal cycles of precipitation and extreme precipitation distributions over several megacities across disparate geographical regions. In general terms, a megacity designates a city with a population of more than 10 million people. In 2018, there were 33 megacities in the world, accounting for 7 % of the world's total population, and the number of megacities is projected to increase to 43 by the year 2030 (UN-DESA, 2018). In the present study, we have selected seven megacities located in diverse geographical regions (Table 1) to examine the forced response of precipitation seasonality and extreme precipitation changes at a local scale for illustrative purposes. This study does not consider the impact of future sea-level rise caused by the thermal expansion of seawater, melting of glaciers and ice sheets, or changes in groundwater storage (Church et al., 2011). Our simulations project substantial changes in precipitation seasonality in terms of its phase and strength. In Tokyo (Japan), which was the world's most populous city in 2018, the phase of precipitation seasonality is projected to remain relatively stable from the historical period through the 25th century. However, the magnitudes of the two peaks are expected to increase in the post-2100 period (Fig. 6 and Fig. S3a). Meanwhile, in São Paulo (Brazil), the wet season

in the current climate state spans from October through March (Silva Dias et al., 2013), but in the future June-October are projected to become the months which have the largest precipitation, with a notable increase in precipitation magnitude from the 23rd century onward (Fig. 6 and Fig. S3b). A similar phase shift is projected to occur in Moscow (Russia) which is currently the northernmost megacity in 2018. Our extended simulations indicate that after the mid-22nd century, summer precipitation

320   will decrease, while winter precipitation is projected to double relative to the historical period (i.e., 1850-1949). As a result, the patterns of wet summers and dry winters will be reversed (Fig. 6 and Fig. S3g). New York (United States) also indicates a strong increase in future winter precipitation (Fig. 6 and Fig. S3e). In addition to these cities depicted in Fig. 6, more generally the Northern Hemisphere high-latitude regions will experience strong increases in winter mean precipitation (Fig. S1f).

The analysis also identifies delayed peaks in the seasonal cycle for some megacities. From the historical period to the 25th
325   century, a peak shift from July to August is apparent for Mumbai (India), and it is accompanied by a nearly two-fold increase in the maximum monthly precipitation (Fig. 6 and Fig. S3d). Our simulations suggest that sustained anthropogenic warming could bring drier conditions to Mexico City (Mexico), with delayed peaks in July and October during the 25th century, compared to peaks in June and September over the period 1850-1949 (Fig. 6 and Fig. S3c). Lagos (Nigeria) presents, in general, a wet season from April to October and a dry season from November to March in the present-day climate (Guo et al., 2022).
330   In the extended future, the precipitation peak in July is projected to shift to September, and this peak will be weakened after the 23rd century with an overall decreasing trend (Fig. 6 and Fig. S3f). Our results point to the heterogeneity of the shifts in the seasonal cycle of precipitation across different regions, highlighting the diverse impacts of Earth's changing climate at the regional-to-urban scales.

Although there are differences in the shape and magnitude of precipitation seasonality changes among the selected megacities,
335   future changes in extreme precipitation exhibit a consistent trend across all locations (Fig. 6). In other words, the likelihood of extreme daily precipitation will increase in the future with sustained greenhouse warming (Giorgi et al., 2019; Gründemann et al., 2022). For instance, in Tokyo the probability of heavy precipitation exceeding 250 mm day^{-1} is projected to increase by an order of magnitude. As the seasonal cycle of precipitation and frequency of extreme events can directly and indirectly impact human activities, water resource management, and the availability of food security, further studies on precipitation seasonality
340   and identifying hot spots of weather extremes are essential.
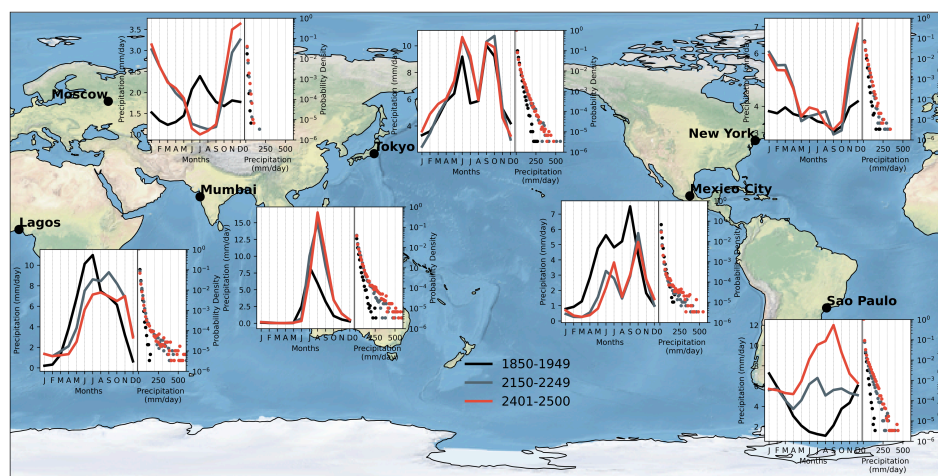
Figure 6: Seasonal cycle of monthly precipitation (solid lines, mm day^{-1}) and probability density function of daily precipitation (dots, %) for seven megacities (Tokyo, São Paulo, Mexico City, Mumbai, New York, Lagos, and Moscow) over the period 1850-1949
345   **(black), 2150-2249 (gray), and 2401-2500 (red). For more details on the seven selected megacities, see Table 1.**

Table 1 Megacities (total population above 10 million) that are selected in the present study.

City	Country	Region	Population (UN-DESA, 2018)
Tokyo	Japan	East Asia	37,468,000
São Paulo	Brazil	South America	21,650,000
Mexico City	Mexico	North America	21,581,000
Mumbai	India	South Asia	19,980,000
New York	United States	North America	18,819,000
Lagos	Nigeria	West Africa	13,463,000
Moscow	Russia	Europe	12,410,000

350

Another key variable that is projected to undergo fundamental changes in seasonality is the surface ocean partial pressure of CO_2 (pCO_2). Although there is disagreement in the amplitude and phase of the seasonal variations in pCO_2 between the climate models and observation-based products, which can be attributed largely to differences in the seasonal variability of the surface

355   dissolved inorganic carbon (DIC) concentrations (Rodgers et al., 2023), an increasing trend in the amplitude of the seasonal cycle of pCO_2 has been addressed in several studies (e.g., Joos et al., 2023; Rodgers et al., 2008). It is also noted that the amplitude of global ocean pCO_2 seasonality is expected to intensify by a factor of 1.5 to 3 over the 2080-2100 period relative to 2006-2026 (Gallego et al., 2018). However, it remains unclear how the pCO_2 seasonality may change beyond 2100. From the historical period to the 25th century across all latitude bands, we identify an intensification of the pCO_2 seasonal cycle

360   amplitude (i.e., maximum minus minimum) (Fig. 7), except for the tropics. The future amplification in pCO_2 seasonality can be attributed to the increased sensitivity of ocean pCO_2 to changes in DIC and temperature contributions (e.g., Gallego et al., 2018), or equivalently to the invasion flux of anthropogenic carbon amplifying the thermally-driven component of the seasonal cycle in pCO_2 (Fassbender et al., 2022). Seasonal variability of pCO_2 in the tropics is small during the historical period, consistent with observation and CMIP6 simulations (Joos et al., 2023), and the tropical ocean still shows weak seasonality

365   beyond 2100 (Fig. 7c). North of 40°N, the timing of maxima and minima in the projected seasonal cycle in the post-2100 period differs remarkably from the seasonality in the historical period, showing earlier occurrence of seasonal minimum and maximum oceanic pCO_2 around April to July, respectively. In the Southern Ocean, the peak in March-April after the end of the 21st century can be attributed to the increasing influence of temperature over DIC (Gallego et al., 2018).
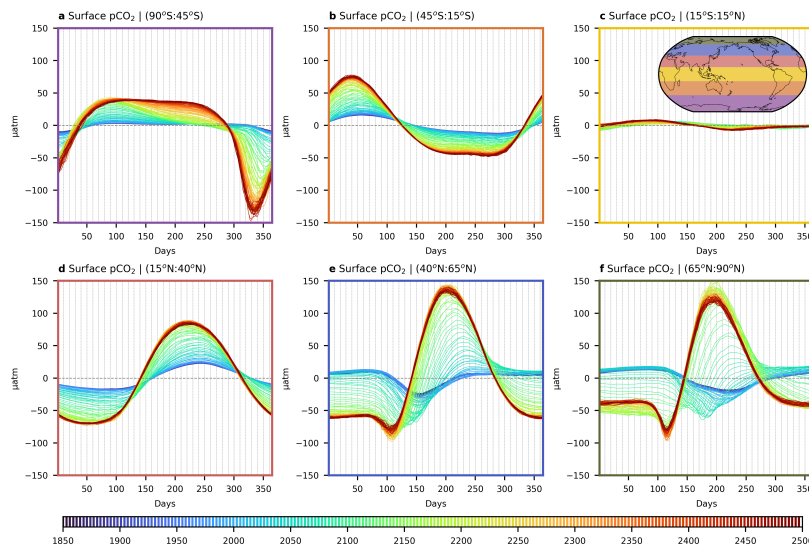
Figure 7: Seasonal cycle of ocean pCO$_2$ (μatm) along latitudinal bands in 5-year intervals. (a) 90°S-45°S, (b) 45°S-15°S, (c) 15°S-15°N, (d) 15°N-40°N, (e) 40°N-65°N, and (f) 65°N-90°N.

3.3 Changes in terrestrial and marine ecosystems and potential carbon-climate feedbacks

Several studies have previously considered carbon-climate feedbacks based on model simulations and observations (Friedlingstein and Prentice, 2010; Koven et al., 2022; Friedlingstein et al., 2006), but uncertainty in quantifying climate-carbon cycle feedbacks in the post-2100 period is still large. Here, we consider broadly future changes in terrestrial and marine ecosystems, as well as the potential carbon-climate feedbacks, based on our extended simulations. Figure 8 illustrates the temporal and spatial changes in total terrestrial carbon stored in soils and vegetation, which can play a vital role in the terrestrial biosphere. The global terrestrial carbon stocks increase from 856 PgC in 2000 to 2288 PgC in 2200, and then decrease to 2079 PgC by 2500 (Fig. 8a). The spatial map shows a notable decrease in terrestrial carbon in parts of the subarctic and Arctic regions, central Africa, and southern Brazil, while showing an increase in the Amazon, Indonesia, parts of Asia, the United States, and southern Canada during the 25th century relative to 1850-1949 (Fig. 8g). The decreasing trend in terrestrial carbon after the 22nd century is largely driven by changes in soil carbon stocks (Fig. 8b, h). A substantial loss of soil carbon occurs after the mid-22nd century, which is consistent with the timing of permafrost disappearance (Fig. 2g). Soils in the permafrost regions contain an enormous amount of organic carbon (Fig. 8e), which has the potential to be released into the atmosphere as carbon dioxide and methane (e.g., Schuur et al., 2015). Even though there may be a strong positive feedback of permafrost carbon to the global climate (Natali et al., 2021), atmospheric radiation computations in our model use prescribed atmospheric CO$_2$ mixing ratios, and thereby carbon released from thawing soil in permafrost regions is not feeding back into the atmospheric radiation budget. This is due to the fact that we follow the CMIP6 convention of following a concentration - rather than an emissions - forcing for our simulations. Based on a coupled model of intermediate complexity which includes a fully coupled representation of oceanic and terrestrial carbon cycle, it is estimated that carbon-climate feedbacks could result in an additional warming of 0.13-1.69 °C by 2300, which is independent of the pathway of anthropogenic emissions (MacDougall et al., 2012). In the deep future period, global soil carbon continues to decline at a similar rate, implying a cumulative additional warming that could be twice as large as the current estimated range of 0.13-1.69 °C by the year 2500. Changes in the soil carbon in the deep future over the tropical and mid-latitude bands are relatively small compared to the changes over the Arctic and subarctic regions (Fig. S4a-c). The global vegetation carbon stock increases from 494 PgC in 2000 to 873 PgC in 2200,

which can be attributed to CO_2 fertilization effects (Fig. 8c). After reaching 900 PgC in 2250, the vegetation carbon stock declines slightly, which is consistent with the temporal evolution of atmospheric CO_2 concentrations (Fig. 1b). Meanwhile, in the high and mid-latitudes of the Northern Hemisphere, the vegetation carbon storage increases by a factor of two (Fig. S4d).

400 Notably, vegetation carbon strongly increases in the Amazon and Indonesian rainforests, while a decrease occurs in the African rainforest. The observed saturation and decline of carbon sinks in tropical forests (Koch et al., 2021), along with our findings, would have implications for the potential future contribution of vegetation carbon losses to atmospheric CO_2 levels.
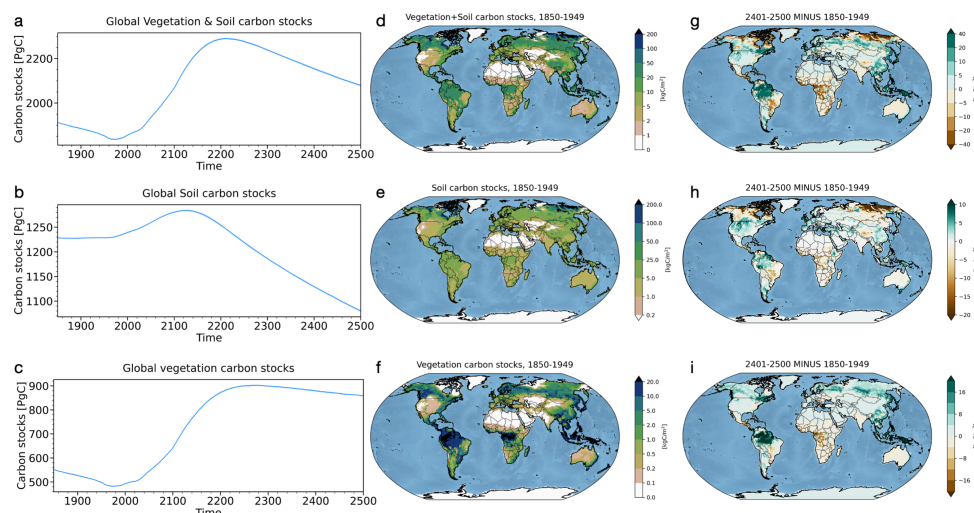
405 **Figure 8: Global (a) vegetation and soil carbon stocks (PgC), (b) soil carbon stocks (PgC), and (c) vegetation carbon stocks (PgC). Climatology (period 1850-1949) for (d) vegetation and soil carbon stocks (kgC m⁻²), (e) soil carbon stocks (kgC m⁻²), and (f) vegetation carbon stocks (kgC m⁻²). Future changes for (g) vegetation and soil carbon stocks (kgC m⁻²), (h) soil carbon stocks (kgC m⁻²), and (i) vegetation carbon stocks (kgC m⁻²) for the period 2401-2500 relative to 1850-1949.**

410

Next, we revisit the approximately 15 % drop in globally integrated marine NPP shown in Fig. 2e. Regionally, ocean NPP increases by up to ~80 % in the Southern Ocean and decreases by up to 50 % in the mid-latitudes of the North Atlantic in the extended future (Fig. 9b). The spatial patterns of NPP change are qualitatively similar to the changes in particulate organic carbon (POC) export in the upper 100 m (Fig. 9e), and the regional increases and decreases in each of NPP and POC export

415 tend to amplify towards the 25th century (Fig. 9c, f), in response to persistent changes in ocean overturning and associated stratification changes. Over the polar regions, large reductions in sea ice cover can increase light and nutrient availability and lengthen the growing seasons of phytoplankton, both of which result in increasing NPP. Over broad areas of the Southern Ocean, where a pronounced projected increase in NPP is evident, enhanced productivity in the surface ocean is co-located with nutrient trapping within the upwelling-dominated Southern Ocean, further fueling NPP (Moore et al., 2018). In contrast,

420 NPP declines in oligotrophic gyres and in the Northern Hemisphere mid-latitudes. The largest decrease identified over the North Atlantic can be attributed to reductions in nutrient concentrations associated with AMOC slowing and oligotrophication of the subpolar North Atlantic, along with increased ocean stratification (Fig. 2). The NPP reductions in oligotrophic gyres are also caused by depletion in surface nutrients, indicating that nutrient uptake plasticity, which plays a key role in sustaining ocean NPP until the 21st century (Kwon et al., 2022), is not as effective beyond the 21st century.

425
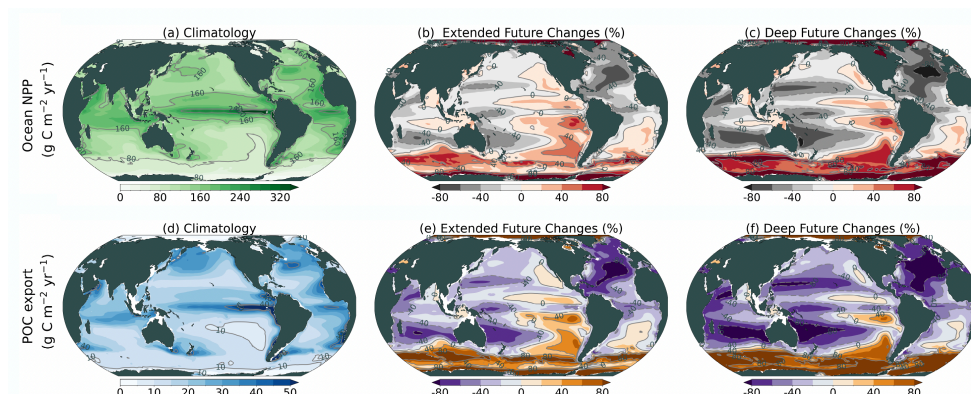
Figure 9: Reference climatology (period 1850-1949) (first column), and future perturbations over the period 2150-2249 (second column) and over the period 2401-2500 (third column), relative to 1850-1949. (a-c) Ocean NPP (gC m^{-2} yr^{-1}) and (d-f) POC export (gC m^{-2} yr^{-1}).

430

To interpret the changes in projected global biogeochemical cycles shown in Fig. 9, it is instructive to consider the relative projected changes in both dissolved inorganic phosphate (PO$_4$) and dissolved inorganic nitrate (NO$_3$) concentrations integrated over the euphotic zone depth which we approximate by averaging over the 0-100 m depth interval for each case. We consider

435 the future changes as fractional changes relative to the model state averaged over the interval 1850-1949. Our simulations reveal broad decreases in PO$_4$ in the extended future, with the largest reductions throughout the subtropical regions (Fig. 10a). Projected changes in NO$_3$ contrast with the changes in PO$_4$, as NO$_3$ shows a patchwork of both increases and decreases across different global regions (Fig. 10c). By the 25th century, relative PO$_4$ concentrations in the euphotic zone are depleted to very low levels throughout the subtropics, as well as across the subpolar North Atlantic and Arctic (Fig. 10b). In contrast, NO$_3$

440 exhibits an even more pronounced pattern of strong increases and decreases in concentrations across different regions (Fig. 10d). These results indicate that, over the full latitudinal range spanned by the shallow overturning subtropical cells, approximately 45°S-40°N, there will be a transition to PO$_4$-limitation for primary production under future climate change. Unlike PO$_4$, a future increase in dissolved inorganic iron (Fe) is evident, except in high-latitude regions of both hemisphere (Fig. 10e, f). The spatial patterns of dissolved inorganic silicate (SiO$_3$) changes are similar to those of NO$_3$, featuring a weak

445 increase in low and mid latitudes and a strong decrease in high-latitude regions (Fig. 10g, h).
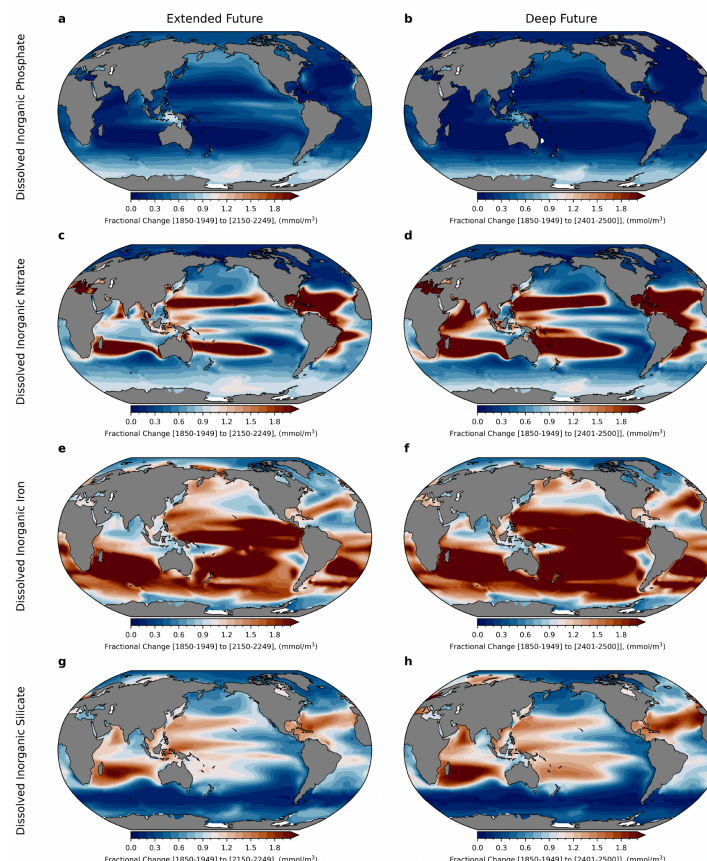
Figure 10: The fractional changes in the period 2150-2249 (first column) and period 2401-2500 (second column) relative to the period 1850-1949. (a, b) PO₄ (mmol m⁻³), (c, d) NO₃ (mmol m⁻³), (e, f) Fe (mmol m⁻³), and (g, h) SiO₃ (mmol m⁻³). The fractional changes were calculated by dividing the values in the future periods by the values in the period 1850-1949. Blue (<1.0) and red (>1.0) indicate future decreases and increases, respectively, relative to the period 1850-1949. All values are averaged over the upper 100 m depth.

We further examined the changes in the vertical structure of PO_4 and NO_3 (Fig. 11). The future changes indicate a substantial decrease in thermocline PO_4 concentrations over the course of the simulations (Fig. 11b, c). The zonally averaged fractional changes in NO_3 concentrations show patches of increasing NO_3 concentrations in surface subtropical regions and more modest decreases in the mesopelagic domain and higher latitudes (Fig. 11e, f). To understand the cause of the changes in zonally averaged PO_4 shown in Fig. 11, we adopt the diagnostic approach applied by Rodgers et al. (2024). This approach considers the transfer efficiency of the mesopelagic domain by analyzing the ratio of fluxes at 1000 m to the fluxes at 100 m. Considered globally, the transfer efficiency for carbon over the recent historical period is approximately 13 % (Table 2). This value falls well within the uncertainty range provided by Doney et al. (2024), which they give as 12.2 ± 4.1 %. For both carbon and PO_4, the transfer efficiency changes only slightly by the end of the 25ᵗʰ century, stabilizing with a modest increase to a global value of approximately 14 %. Viewed this way, the mesopelagic remineralization source shows substantial changes in the deep future, with decreases by the 2490s for carbon being 28.4 % and for PO_4 being 36.0 % (Table 2).

Notably, three key points should be emphasized regarding these changes in mesopelagic remineralization. First, the reduced rate of remineralization for PO_4 is consistent in sign with the projected decreases in zonally averaged PO_4 for the mesopelagic domain (Fig. 11b, c). Second, the fractional loss in PO_4 remineralization is greater than that for DIC. This characteristic of the plastic stoichiometric relationship between carbon and phosphate in MARBL indicates that the forced changes identified for

PO$_4$ are partially buffered in the case of carbon. This buffering or damping effect is approximately 20 % by the 2490s for the globally integrated impact. Third, despite warming of the mesopelagic domain for these simulations, the MARBL
470 biogeochemistry does not respond with enhanced remineralization in response to increasing in situ temperatures. Consequently, this model does not provide a negative feedback through shoaling of the effective remineralization depth in response to mesopelagic warming that may compensate for decreases in export production in response to decreased overturning and increased stratification (Rodgers et al., 2024). Further analysis over the 30°S-30°N region shows that mesopelagic remineralization losses in this region are larger than the global mean, specifically 45.6 % for carbon and 53.8 % for PO$_4$ by the
475 2490s (Supplementary Table 1). In contrast, for the Southern Ocean domain spanning 90°S-60°S, mesopelagic remineralization sources for both carbon and PO$_4$ increase by 141 % by the 2490s (Supplementary Table 2). The results illustrate a contrast between these regions of reduced ocean overturning circulation, revealing opposite signs in their long-term responses. For the Southern Ocean, the response is thought to reflect changes in iron availability resulting from sea ice retreat (Moore et al., 2018). Interestingly, the modest buffering of the carbon mesopelagic remineralization source relative to PO$_4$ by
480 plastic stoichiometry observed in low-latitude regions is not evident in the Southern Ocean region.
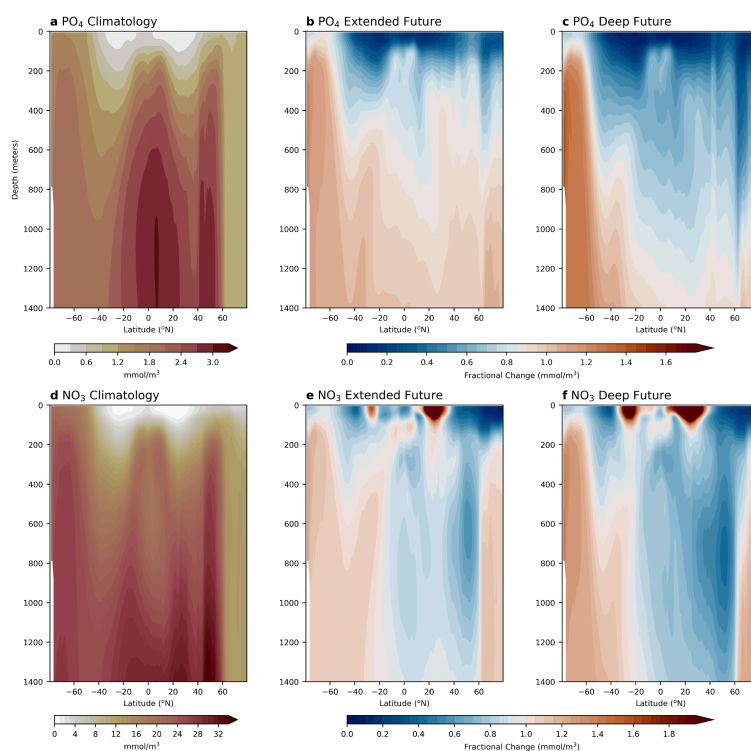
Figure 11: Reference climatology (period 1850-1949) (first column), and fractional changes in the period 2150-2249 (second column) and period 2401-2500 (third column), relative to 1850-1949. (a-c) Zonally averaged PO$_4$ (mmol m^{-3}) and (d-f) zonally averaged NO$_3$
485 **(mmol m^{-3}). The fractional changes were calculated by dividing the values in the future periods by the values in the period 1850-1949. Blue (<1.0) and red (>1.0) in b, c, e and f indicate future decreases and increases, respectively, relative to the period 1850-1949.**

490

Table 2 The centennial-timescale ensemble-mean retention of mesopelagic (100 m-1000 m) carbon and PO$_4$ (italic and bold) over the global ocean domain. Fluxes of soft tissue at 100 m (F$_{100}$) and 1000 m (F$_{1000}$) represent fluxes at the top and bottom of the mesopelagic domain. Ten-year averages for each quantity are calculated over the 1890s, 1990s, 2090s, 2190s, 2290s, 2390s, and 2490s to minimize interannual variability beyond the 10-member ensemble average. Transfer efficiency is defined as the ratio of the fluxes at 1000 m and 100 m (F$_{1000}$/F$_{100}$), following Doney et al. (2024) The remineralization source is given as the difference between the fluxes at 100 m 1000 m (F$_{100}$ - F$_{1000}$). For each case, the numbers given in parentheses are the percentage changes relative to the 1890s.

GLOBAL DIC *PO$_4$*	F$_{100}$ (PgC yr^{-1}) *(TmolPO$_4$ yr^{-1})*	F$_{1000}$ (PgC yr^{-1}) *(TmolPO$_4$ yr^{-1})*	Transfer efficiency	Mesopelagic Accumulation (Remineralization source) (PgC yr^{-1}) *(TmolPO$_4$ yr^{-1})*
1890s	6.98 *4.57*	0.936 *0.621*	0.134 *0.136*	6.04 *3.95*
1990s	7.08 (+1.4%) *4.61 (+0.8%)*	0.945 (+0.9%) *0.627 (+0.9%)*	0.134 *0.136*	6.13 (+1.5%) *3.98 (+0.7%)*
2090s	6.91 (-1.1%) *4.27 (-6.6%)*	0.996 (+6.3%) *0.623 (+0.3%)*	0.144 *0.146*	5.91 (-2.2%) *3.65 (-7.7%)*
2190s	5.85 (-16.2%) *3.48 (-23.9%)*	0.862 (-8.0%) *0.512 (-17.6%)*	0.147 *0.147*	4.99 (-17.5%) *2.97 (-24.8%)*
2290s	5.43 (-22.2%) *3.19 (-30.2%)*	0.795 (-15.1%) *0.464 (-25.3%)*	0.146 *0.145*	4.63 (-23.3%) *2.73 (-31.0%)*
2390s	5.21 (-24.5%) *3.05 (-33.3%)*	0.759 (-18.9%) *0.440 (-29.2%)*	0.146 *0.144*	4.45 (-26.4%) *2.61 (-34.0%)*
2490s	5.06 (-27.6%) *2.95 (-35.5%)*	0.732 (-21.8%) *0.422 (-32.0%)*	0.145 *0.143*	4.33 (-28.4%) *2.53 (-36.0%)*

Finally, diagnostics were performed of the export ratio for biogeochemical fluxes, defined as the ratio of the sinking or export production flux to NPP (Supplementary Table 3). Over the global domain, the ensemble-mean value for the 1990s in our simulations is 0.145. This falls within the uncertainty bounds of the levels presented by Doney et al. (2024), which are 0.154 ± 0.026 for the forced ocean biogeochemical models included in the REgional Carbon Cycle Assessment and Processes (RECCAP2) project. This ratio over the global domain decreases by 16.6 % by the 2490s, indicating that nutrient recycling in the euphotic zone is enhanced over time. In the 30°S-30°N domain, the decrease of 24.0 % by the 2490s is larger than the global mean reduction. This result is consistent in sign with the finding for the earlier CESM1 simulations under similarly strong CMIP5 forcing (Moore et al., 2018), although the reason for a decreasing export ratio under reduced primary production remains unclear. It is worth noting that the extratropics of the Southern Hemisphere (90°S-30°S) and Northern Hemisphere (30°N-90°N) show quite different trends. The export ratio decreases by only 4.8 % in the Southern Hemisphere extratropics, while it decreases by 28.1 % in the Northern Hemisphere extratropics.

We further examined the evolution and the spatial patterns of ocean carbon uptake in response to greenhouse warming. The global integral of ocean carbon uptake shows a peak in approximately 2100 in excess of 4 PgC yr^{-1}, followed by an exponential decline to less than 1 PgC yr^{-1} by 2500 (Fig. 2f, Fig. 12a). Until the 23rd century, the uptake over the latitude range of the subtropical cells (45°S-40°N) contributes at least half of the total uptake, however, by 2500, this contribution diminishes to less than 25 %. The Southern Ocean (90°S-45°S) accounts for about 25 % of the total uptake at the end of the 21st century, then this contribution increases to nearly half of the global uptake by 2500. The northern latitudes (40°N-90°N) show peak uptake during the 21st century, but then decline to less than 0.5 PgC yr^{-1} after 2200. To better understand the changes in ocean carbon uptake, we investigated the DpCO$_2$ distribution (difference in pCO$_2$ between the ocean and atmosphere). During the

historical reference period 1850-1949, the thermodynamic gradient in pCO$_2$ driving CO$_2$ outgassing was largest for the equatorial and eastern boundary upwelling regions of the Pacific and Indian Oceans (Fig. 12b), whereas for the deep future

525 period this distribution shifts, extending further into the Indian Ocean and showing maxima near 20° latitude in both hemispheres (Fig. 12c). To shed light onto how changes in the ocean state impact the natural carbon cycle, we examined the CO$_2$ fluxes for RAD (radiatively coupled forcing). Instead of a gradual change towards warming-induced CO$_2$ outgassing, the global integral shows a shift towards net outgassing of natural carbon, a shift which occurs predominantly between 2100 and 2200 (Fig. 12d). This decline is largely driven by a longer-term trend towards net outgassing in the subtropical regions, with

530 a smaller contribution that occurs earlier in the northern high latitudes. In contrast, the Southern Ocean shows a shift towards enhanced CO$_2$ uptake after the 22nd century. To gain further insight into the patterns associated with these changes, we analyzed the DpCO$_2$ for the RAD case. This analysis reveals a shift towards broad CO$_2$ outgassing over the region spanning 30°S-30°N (Fig. 12f). Since this natural carbon tracer only sees pre-industrial atmospheric CO$_2$ levels through the gas exchange by construction, this shift to outgassing is indicative of a positive climate feedback by the marine carbon cycle, operating through

535 the natural carbon cycle, that could counteract the overall carbon uptake shown in Fig. 12a.
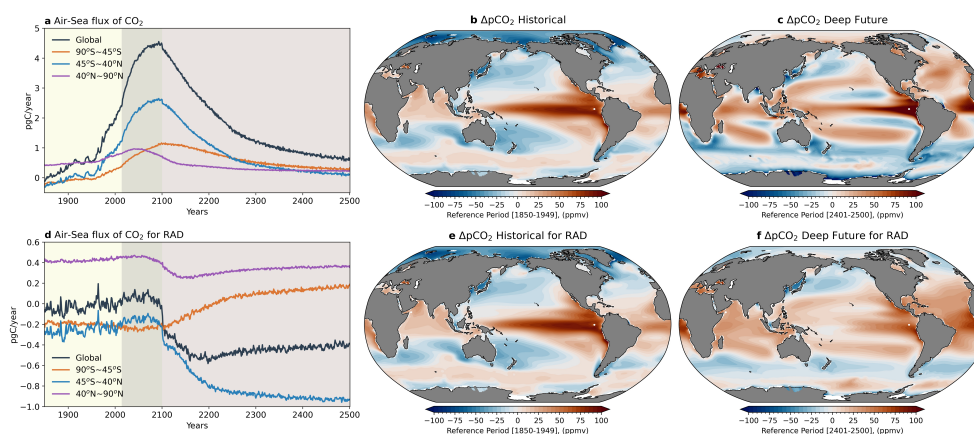
Figure 12: Changes in surface ocean carbon state and fluxes. (a) Spatially integrated air-sea CO$_2$ fluxes (PgC year^{-1}) for the ensemble mean considered globally (black), 90°S-45°S (orange), over 45°S-40°N (blue), and over 40°N-90°N (purple), where a 12-month

540 **running mean has been applied to the ensemble mean to remove seasonal variations, and positive values indicating ocean uptake of carbon. (b) ΔpCO$_2$ (ppmv) averaged over the 1850-1949, taken as the difference between oceanic and atmospheric pCO$_2$ and (c) ΔpCO$_2$ averaged over the 2401-2500. Positive values occur where there is outgassing. (d-f) Same as (a-c) except for RAD case (i.e., the system is radiatively coupled, but pre-industrial CO$_2$ concentrations are maintained for air-sea gas exchange).**

4. Summary and Discussion

545 Sustained anthropogenic warming has widespread and profound impacts on the Earth's climate system, and understanding these effects beyond 2100 is crucial for highlighting potential future natural disaster risks and assessing long-term climate sensitivity. To explore multi-centennial responses to sustained warming over the next few centuries, we have conducted new long-term ensemble simulations which extend 10 members of CESM2-LE to the year 2500. Our unprecedented fully coupled simulations provide insights into changes in the mean state and variability for key fields across the atmosphere, ocean, sea ice,

550 land, and ecosystems on multi-centennial time scales from 1850 to 2500. Additionally, we discuss potential carbon-climate feedbacks that may emerge beyond 2100.

Over the period 1850-2500, our extended simulations indicate a strong greenhouse warming of greater than 12 °C by the end of the 25th century relative to the historical period, despite the fact that fossil and industrial CO$_2$ emissions are effectively reduced to zero by 2250 under the extended SSP3-7.0 scenario. By the 25th century, the eastern equatorial Pacific is projected

555 to warm by 8-10 °C relative to the historical reference period 1850-1949. This warming will be accompanied by weakened easterlies, intensified atmospheric upward motion over the whole equatorial Pacific sector, and increased precipitation within a narrower latitudinal range characterized by a northward shift of SPCZ with a loss of its diagonal orientation toward the subtropics (Fig. 3). These changes in the mean state will substantially alter ocean-atmosphere interactions, including the Pacific Walker circulation. In addition to the mean precipitation changes, at a local scale, extreme precipitation events are projected

560 to become more frequent across different geographical regions, while diverse changes in the timing and intensity in the seasonal distribution of precipitation are projected to occur (Fig. 6), indicating heterogeneous impacts of climate change at regional and urban levels.

Amplified warming in the Northern Hemisphere high-latitudes will drive permafrost thawing, which is a major pathway for loss of soil carbon after the mid-22nd century, and thus the land will subsequently become a source of CO_2. However, on multi-

565 centennial timescales, the global ocean still acts as a sink for anthropogenic carbon, with the increases of Southern Ocean's contribution from 25 % to nearly 50 % by 2500 (Fig. 12), although continuous reduction of ocean carbon uptake is projected from the 22nd century due to decreases in the CO_2 buffering capacity of seawater. Our CESM2-LE extension simulations under SSP3-7.0, consistent with the findings of Rodgers et al. (2024) for projections with CESM2-WACCM to 2299 under SSP5-8.5 forcing, project a substantial depletion of PO_4 in the low-latitude mesopelagic domain, along with a modest increase in the

570 transfer efficiency. This response of decreasing PO_4 remineralization is buffered or damped by approximately 20 % for carbon remineralization, indicating that the stoichiometric plasticity mechanism identified by Kwon et al. (2022) provides only moderate modulation into the deep future. The projected future changes in nutrient dynamics could affect primary productivity, food webs, and biodiversity in marine ecosystems.

Through analyses focused on how sustained warming can impact variance within the Earth system, we identified decreases in

575 surface temperature variability across most regions except Africa, Asia, Australia, South America, and the North Atlantic. In contrast, precipitation variability is projected to increase in most areas, particularly in the tropics where the merging of precipitation bands amplifies variability. The model projects substantial reductions in ENSO variability beyond 2100, but precipitation variability in the Niño3.4 region shows a rebound in variability after the mid-23rd century. In contrast to ENSO variability changes, the intensity of the MJO is projected to strengthen notably, making it a key player in representing

580 variability in the tropical region during the post-2100 period (Fig. 5).

The forced responses in mean state and variability in the system presented here provide a broad view of how long-term greenhouse warming affects not only the average climate conditions but also variability and extremes across different spatial and temporal scales. Additionally, this study could serve as a foundational step toward understanding multi-century climate-carbon feedbacks. Further complementary simulations are needed to explore these potential feedbacks more thoroughly.

585 Although the future climate projections beyond 2100 are influenced by multiple factors such as the climate sensitivity of models and the choice of emission scenarios, it is apparent that there is an urgent need for drastic reductions in carbon emissions from human activities. Our study indicates that developing long-term mitigation policies based on the post-2100 perspective is not mature.

590

Code availability

The CESM2 code is available from https://www.cesm.ucar.edu/models/cesm2. Scripts and data to reproduce the figures and

595   analysis of this paper can be found at https://climatedata.ibs.re.kr/data/papers/lee-et-al-2024-earth-system-dynamics (will be

updated after review).

Data availability

All datasets used in the study are publicly available. CESM2-LE extension simulations datasets are available on ICCP Climate

600   Data Website (will be in https://ibsclimate.org after review).

Author contributions

The model simulations were set up and performed through a collaborative effort by S.-S.L. and N.R. The scientific framework

of this manuscript was developed by S.-S.L., S.S and K.B.R.. All authors discussed the results and contributed to the analysis

605   and writing of the manuscript.

Competing interests

At least one of the (co-)authors is a member of the editorial board of Earth System Dynamics.

Acknowledgements

610   We thank A. Timmermann, Gokhan Danabasoglu, Keith Lindsay, and Michael Mills for their valuable comments, discussions

and support throughout this work. This work was supported by the Institute for Basic Science (IBS), Republic of Korea, under

IBS-R028-D1. The simulations presented here were carried out on the IBS/ICCP supercomputer "Aleph", a 1.43 petaflop high-

performance Cray XC50-LC Skylake computing system with 18,720 processor cores, 9.59 PB of disc storage, and 43 PB of

615   tape archive storage. We also acknowledge the support of KREONET.

References

Adler, R. F., Gu, G., and Huffman, G. J.: Estimating climatological bias errors for the Global Precipitation Climatology Project
620   (GPCP), Journal of Applied Meteorology and Climatology, 51, 84-99, 2012.
Adler, R. F., Huffman, G. J., Chang, A., Ferraro, R., Xie, P.-P., Janowiak, J., Rudolf, B., Schneider, U., Curtis, S., and Bolvin,
      D.: The version-2 global precipitation climatology project (GPCP) monthly precipitation analysis (1979–present),
      Journal of hydrometeorology, 4, 1147-1167, 2003.
Archer, D., Eby, M., Brovkin, V., Ridgwell, A., Cao, L., Mikolajewicz, U., Caldeira, K., Matsumoto, K., Munhoven, G.,
625   Montenegro, A., and Tokos, K.: Atmospheric Lifetime of Fossil Fuel Carbon Dioxide, Annual Review of Earth and
      Planetary Sciences, 37, 117-134, 2009.
Armour, K. C., Marshall, J., Scott, J. R., Donohoe, A., and Newsom, E. R.: Southern Ocean warming delayed by circumpolar
      upwelling and equatorward transport, Nature Geoscience, 9, 549-554, 2016.
Bailey, D. A., Holland, M. M., DuVivier, A. K., Hunke, E. C., and Turner, A. K.: Impact of a New Sea Ice Thermodynamic
630   Formulation in the CESM2 Sea Ice Component, Journal of Advances in Modeling Earth Systems, 12,
      e2020MS002154, https://doi.org/10.1029/2020MS002154, 2020.
Bellomo, K., Angeloni, M., Corti, S., and von Hardenberg, J.: Future climate change shaped by inter-model differences in
      Atlantic meridional overturning circulation response, Nature Communications, 12, 3659, 10.1038/s41467-021-
      24015-w, 2021.
635   Cai, W., Lengaigne, M., Borlace, S., Collins, M., Cowan, T., McPhaden, M. J., Timmermann, A., Power, S., Brown, J., and
      Menkes, C.: More extreme swings of the South Pacific convergence zone due to greenhouse warming, Nature, 488,
      365-369, 2012.
Cai, W., Santoso, A., Collins, M., Dewitte, B., Karamperidou, C., Kug, J.-S., Lengaigne, M., McPhaden, M. J., Stuecker, M.
      F., Taschetto, A. S., Timmermann, A., Wu, L., Yeh, S.-W., Wang, G., Ng, B., Jia, F., Yang, Y., Ying, J., Zheng, X.-
640   T., Bayr, T., Brown, J. R., Capotondi, A., Cobb, K. M., Gan, B., Geng, T., Ham, Y.-G., Jin, F.-F., Jo, H.-S., Li, X.,
      Lin, X., McGregor, S., Park, J.-H., Stein, K., Yang, K., Zhang, L., and Zhong, W.: Changing El Niño–Southern
      Oscillation in a warming climate, Nature Reviews Earth & Environment, 2, 628-644, 10.1038/s43017-021-00199-z,
      2021.

645 Callahan, C. W., Chen, C., Rugenstein, M., Bloch-Johnson, J., Yang, S., and Moyer, E. J.: Robust decrease in El Niño/Southern Oscillation amplitude under long-term warming, Nature Climate Change, 11, 752-757, 2021.

Chadwick, R., Boutle, I., and Martin, G.: Spatial Patterns of Precipitation Change in CMIP5: Why the Rich Do Not Get Richer in the Tropics, Journal of Climate, 26, 3803-3822, https://doi.org/10.1175/JCLI-D-12-00543.1, 2013.

Cheng, L., Abraham, J., Hausfather, Z., and Trenberth, K. E.: How fast are the oceans warming?, Science, 363, 128-129, doi:10.1126/science.aav7619, 2019.

650 Cheng, L., von Schuckmann, K., Abraham, J. P., Trenberth, K. E., Mann, M. E., Zanna, L., England, M. H., Zika, J. D., Fasullo, J. T., Yu, Y., Pan, Y., Zhu, J., Newsom, E. R., Bronselaer, B., and Lin, X.: Past and future ocean warming, Nature Reviews Earth & Environment, 3, 776-794, 10.1038/s43017-022-00345-1, 2022.

Chikamoto, M. O. and DiNezio, P.: Multi-Century Changes in the Ocean Carbon Cycle Controlled by the Tropical Oceans and the Southern Ocean, Global Biogeochemical Cycles, 35, e2021GB007090, 2021.

655 Chung, E.-S., Timmermann, A., Soden, B. J., Ha, K.-J., Shi, L., and John, V. O.: Reconciling opposing Walker circulation trends in observations and model projections, Nature Climate Change, 9, 405-412, 10.1038/s41558-019-0446-4, 2019.

Church, J. A., Gregory, J. M., White, N. J., Platten, S. M., and Mitrovica, J. X.: Understanding and projecting sea level change, Oceanography, 24, 130-143, 2011.

Cui, J. and Li, T.: Changes of MJO propagation characteristics under global warming, Climate Dynamics, 53, 5311-5327, 660 10.1007/s00382-019-04864-4, 2019.

Danabasoglu, G., Lamarque, J. F., Bacmeister, J., Bailey, D., DuVivier, A., Edwards, J., Emmons, L., Fasullo, J., Garcia, R., and Gettelman, A.: The community earth system model version 2 (CESM2), Journal of Advances in Modeling Earth Systems, 12, e2019MS001916, 2020.

Davy, R. and Outten, S.: The Arctic Surface Climate in CMIP6: Status and Developments since CMIP5, Journal of Climate, 665 33, 8047-8068, https://doi.org/10.1175/JCLI-D-19-0990.1, 2020.

Deng, K., Azorin-Molina, C., Yang, S., Hu, C., Zhang, G., Minola, L., and Chen, D.: Changes of Southern Hemisphere westerlies in the future warming climate, Atmospheric Research, 270, 106040, https://doi.org/10.1016/j.atmosres.2022.106040, 2022.

Deser, C., Lehner, F., Rodgers, K. B., Ault, T., Delworth, T. L., DiNezio, P. N., Fiore, A., Frankignoul, C., Fyfe, J. C., and 670 Horton, D. E.: Insights from Earth system model initial-condition large ensembles and future prospects, Nature Climate Change, 10, 277-286, 2020.

Ditlevsen, P. and Ditlevsen, S.: Warning of a forthcoming collapse of the Atlantic meridional overturning circulation, Nature Communications, 14, 4254, 10.1038/s41467-023-39810-w, 2023.

Doney, S. C., Mitchell, K. A., Henson, S. A., Cavan, E., DeVries, T., Gruber, N., Hauck, J., Mouw, C. B., Müller, J. D., and 675 Primeau, F. W.: Observational and Numerical Modeling Constraints on the Global Ocean Biological Carbon Pump, Global Biogeochemical Cycles, 38, e2024GB008156, https://doi.org/10.1029/2024GB008156, 2024.

Fassbender, A. J., Schlunegger, S., Rodgers, K. B., and Dunne, J. P.: Quantifying the Role of Seasonality in the Marine Carbon Cycle Feedback: An ESM2M Case Study, Global Biogeochemical Cycles, 36, e2021GB007018, https://doi.org/10.1029/2021GB007018, 2022.

680 Fetterer, F., Knowles, K., Meier, W., Savoie, M., and Windnagel, A: Sea Ice Index, version 3, National Snow and Ice Data Center, 2017.

Frajka-Williams, E., Ansorge, I. J., Baehr, J., Bryden, H. L., Chidichimo, M. P., Cunningham, S. A., Danabasoglu, G., Dong, S., Donohue, K. A., and Elipot, S.: Atlantic meridional overturning circulation: Observed transport and variability, Frontiers in Marine Science, 6, 260, 2019.

685 Fredriksen, H.-B., Berner, J., Subramanian, A. C., and Capotondi, A.: How Does El Niño–Southern Oscillation Change Under Global Warming—A First Look at CMIP6, Geophysical Research Letters, 47, e2020GL090640, https://doi.org/10.1029/2020GL090640, 2020.

Friedlingstein, P. and Prentice, I. C.: Carbon–climate feedbacks: a review of model and observation based estimates, Current Opinion in Environmental Sustainability, 2, 251-257, https://doi.org/10.1016/j.cosust.2010.06.002, 2010.

690 Friedlingstein, P., Cox, P., Betts, R., Bopp, L., von Bloh, W., Brovkin, V., Cadule, P., Doney, S., Eby, M., and Fung, I.: Climate–carbon cycle feedback analysis: results from the C4MIP model intercomparison, Journal of climate, 19, 3337-3353, 2006.

Gallego, M. A., Timmermann, A., Friedrich, T., and Zeebe, R. E.: Drivers of future seasonal cycle changes in oceanic pCO2, Biogeosciences, 15, 5315-5327, 10.5194/bg-15-5315-2018, 2018.

695 Garcia-Soto, C., Cheng, L., Caesar, L., Schmidtko, S., Jewett, E. B., Cheripka, A., Rigor, I., Caballero, A., Chiba, S., and Báez, J. C.: An overview of ocean climate change indicators: Sea surface temperature, ocean heat content, ocean pH, dissolved oxygen concentration, arctic sea ice extent, thickness and volume, sea level and strength of the AMOC (Atlantic Meridional Overturning Circulation), Frontiers in Marine Science, 8, 642372, 2021.

Geng, T., Cai, W., Jia, F., and Wu, L.: Decreased ENSO post-2100 in response to formation of a permanent El Niño-like state 700 under greenhouse warming, Nature Communications, 15, 5810, 10.1038/s41467-024-50156-9, 2024.

Giorgi, F., Raffaele, F., and Coppola, E.: The response of precipitation characteristics to global warming from climate projections, Earth Syst. Dynam., 10, 73-89, 10.5194/esd-10-73-2019, 2019.

Gründemann, G. J., van de Giesen, N., Brunner, L., and van der Ent, R.: Rarest rainfall events will see the greatest relative increase in magnitude under future climate change, Communications Earth & Environment, 3, 235, 10.1038/s43247-705 022-00558-8, 2022.

Guo, L., Di, L., Zhang, C., Lin, L., Chen, F., and Molla, A.: Evaluating contributions of urbanization and global climate change to urban land surface temperature change: a case study in Lagos, Nigeria, Scientific Reports, 12, 14168, 10.1038/s41598-022-18193-w, 2022.

710 Hezel, P. J., Fichefet, T., and Massonnet, F.: Modeled Arctic sea ice evolution through 2300 in CMIP5 extended RCPs, The Cryosphere, 8, 1195-1204, 10.5194/tc-8-1195-2014, 2014.

IPCC: Summary for Policymakers. In: Climate Change 2021: The Physical Science Basis. Contribution of Working Group I to the Sixth Assessment Report of the Intergovernmental Panel on Climate Change [Masson-Delmotte, V., P. Zhai, A. Pirani, S.L. Connors, C. Péan, S. Berger, N. Caud, Y. Chen, L. Goldfarb, M.I. Gomis, M. Huang, K. Leitzell, E. Lonnoy, J.B.R. Matthews, T.K. Maycock, T. Waterfield, O. Yelekçi, R. Yu, and B. Zhou (eds.)]. Cambridge
715 University Press, Cambridge, United Kingdom and New York, NY, USA, pp. 3−32, doi:10.1017/9781009157896.001, 2021.

Ishii, M., Fukuda, Y., Hirahara, S., Yasui, S., Suzuki, T., and Sato, K.: Accuracy of global upper ocean heat content estimation expected from present observational data sets, Sola, 13, 163-167, 2017.

Joos, F., Hameau, A., Frölicher, T. L., and Stephenson, D. B.: Anthropogenic Attribution of the Increasing Seasonal Amplitude
720 in Surface Ocean pCO2, Geophysical Research Letters, 50, e2023GL102857, https://doi.org/10.1029/2023GL102857, 2023.

Koch, A., Hubau, W., and Lewis, S. L.: Earth System Models Are Not Capturing Present-Day Tropical Forest Carbon Dynamics, Earth's Future, 9, e2020EF001874, https://doi.org/10.1029/2020EF001874, 2021.

Koven, C. D., Arora, V. K., Cadule, P., Fisher, R. A., Jones, C. D., Lawrence, D. M., Lewis, J., Lindsay, K., Mathesius, S.,
725 Meinshausen, M., Mills, M., Nicholls, Z., Sanderson, B. M., Séférian, R., Swart, N. C., Wieder, W. R., and Zickfeld, K.: Multi-century dynamics of the climate and carbon cycle under both high and net negative emissions scenarios, Earth Syst. Dynam., 13, 885-909, 10.5194/esd-13-885-2022, 2022.

Kwon, E. Y., Sreeush, M. G., Timmermann, A., Karl, D. M., Church, M. J., Lee, S.-S., and Yamaguchi, R.: Nutrient uptake plasticity in phytoplankton sustains future ocean net primary production, Science Advances, 8, eadd2475,
730 doi:10.1126/sciadv.add2475, 2022.

Lawrence, D. M., Fisher, R. A., Koven, C. D., Oleson, K. W., Swenson, S. C., Bonan, G., Collier, N., Ghimire, B., van Kampenhout, L., Kennedy, D., Kluzek, E., Lawrence, P. J., Li, F., Li, H., Lombardozzi, D., Riley, W. J., Sacks, W. J., Shi, M., Vertenstein, M., Wieder, W. R., Xu, C., Ali, A. A., Badger, A. M., Bisht, G., van den Broeke, M., Brunke, M. A., Burns, S. P., Buzan, J., Clark, M., Craig, A., Dahlin, K., Drewniak, B., Fisher, J. B., Flanner, M., Fox, A. M.,
735 Gentine, P., Hoffman, F., Keppel-Aleks, G., Knox, R., Kumar, S., Lenaerts, J., Leung, L. R., Lipscomb, W. H., Lu, Y., Pandey, A., Pelletier, J. D., Perket, J., Randerson, J. T., Ricciuto, D. M., Sanderson, B. M., Slater, A., Subin, Z. M., Tang, J., Thomas, R. Q., Val Martin, M., and Zeng, X.: The Community Land Model Version 5: Description of New Features, Benchmarking, and Impact of Forcing Uncertainty, Journal of Advances in Modeling Earth Systems, 11, 4245-4287, https://doi.org/10.1029/2018MS001583, 2019.

740 Lee, S., L'Heureux, M., Wittenberg, A. T., Seager, R., O'Gorman, P. A., and Johnson, N. C.: On the future zonal contrasts of equatorial Pacific climate: Perspectives from Observations, Simulations, and Theories, npj Climate and Atmospheric Science, 5, 82, 10.1038/s41612-022-00301-2, 2022.

Liu, W., Fedorov, A. V., Xie, S.-P., and Hu, S.: Climate impacts of a weakened Atlantic Meridional Overturning Circulation in a warming climate, Science Advances, 6, eaaz4876, 10.1126/sciadv.aaz4876,
745 Loeb, N. G., Wielicki, B. A., Doelling, D. R., Smith, G. L., Keyes, D. F., Kato, S., Manalo-Smith, N., and Wong, T.: Toward optimal closure of the Earth's top-of-atmosphere radiation budget, Journal of Climate, 22, 748-766, 2009.

Loeb, N. G., Doelling, D. R., Wang, H., Su, W., Nguyen, C., Corbett, J. G., Liang, L., Mitrescu, C., Rose, F. G., and Kato, S.: Clouds and the earth's radiant energy system (CERES) energy balanced and filled (EBAF) top-of-atmosphere (TOA) edition-4.0 data product, Journal of climate, 31, 895-918, 2018.

750 Long, M. C., Moore, J. K., Lindsay, K., Levy, M., Doney, S. C., Luo, J. Y., Krumhardt, K. M., Letscher, R. T., Grover, M., and Sylvester, Z. T.: Simulations with the marine biogeochemistry library (MARBL), Journal of Advances in Modeling Earth Systems, 13, e2021MS002647, 2021.

MacDougall, A. H., Avis, C. A., and Weaver, A. J.: Significant contribution to climate warming from the permafrost carbon feedback, Nature Geoscience, 5, 719-721, 10.1038/ngeo1573, 2012.

755 Madden, R. A. and Julian, P. R.: Description of global-scale circulation cells in the tropics with a 40–50 day period, Journal of Atmospheric Sciences, 29, 1109-1123, 1972.

Mahowald, N. M., Randerson, J. T., Lindsay, K., Munoz, E., Doney, S. C., Lawrence, P., Schlunegger, S., Ward, D. S., Lawrence, D., and Hoffman, F. M.: Interactions between land use change and carbon cycle feedbacks, Global Biogeochemical Cycles, 31, 96-113, https://doi.org/10.1002/2016GB005374, 2017.

760 Meinshausen, M., Nicholls, Z. R. J., Lewis, J., Gidden, M. J., Vogel, E., Freund, M., Beyerle, U., Gessner, C., Nauels, A., Bauer, N., Canadell, J. G., Daniel, J. S., John, A., Krummel, P. B., Luderer, G., Meinshausen, N., Montzka, S. A., Rayner, P. J., Reimann, S., Smith, S. J., van den Berg, M., Velders, G. J. M., Vollmer, M. K., and Wang, R. H. J.: The shared socio-economic pathway (SSP) greenhouse gas concentrations and their extensions to 2500, Geosci. Model Dev., 13, 3571-3605, 10.5194/gmd-13-3571-2020, 2020.

765 Moore, J. K., Fu, W., Primeau, F., Britten, G. L., Lindsay, K., Long, M., Doney, S. C., Mahowald, N., Hoffman, F., and Randerson, J. T.: Sustained climate warming drives declining marine biological productivity, Science, 359, 1139-1143, 10.1126/science.aao6379, 2018.

Morice, C. P., Kennedy, J. J., Rayner, N. A., and Jones, P. D.: Quantifying uncertainties in global and regional temperature
    change using an ensemble of observational estimates: The HadCRUT4 data set, Journal of Geophysical Research:
770   Atmospheres, 117, 2012.

Natali, S. M., Holdren, J. P., Rogers, B. M., Treharne, R., Duffy, P. B., Pomerance, R., and MacDonald, E.: Permafrost carbon
    feedbacks threaten global climate goals, Proceedings of the National Academy of Sciences, 118, e2100163118,
    10.1073/pnas.2100163118, 2021.

O'Neill, B. C., Tebaldi, C., Van Vuuren, D. P., Eyring, V., Friedlingstein, P., Hurtt, G., Knutti, R., Kriegler, E., Lamarque, J.-
775   F., and Lowe, J.: The scenario model intercomparison project (ScenarioMIP) for CMIP6, Geoscientific Model
    Development, 9, 3461-3482, 2016.

Oh, J.-H., Kug, J.-S., An, S.-I., Jin, F.-F., McPhaden, M. J., and Shin, J.: Emergent climate change patterns originating from
    deep ocean warming in climate mitigation scenarios, Nature Climate Change, 14, 260-266, 10.1038/s41558-024-
    01928-0, 2024.

780 Peng, Q., Xie, S.-P., and Deser, C.: Collapsed upwelling projected to weaken ENSO under sustained warming beyond the
    twenty-first century, Nature Climate Change, 10.1038/s41558-024-02061-8, 2024.

Prentice, I. C., Farquhar, G., Fasham, M., Goulden, M. L., Heimann, M., Jaramillo, V., Kheshgi, H., Le Quéré, C., Scholes, R.
    J., and Wallace, D. W.: The carbon cycle and atmospheric carbon dioxide, Climate change 2001: the scientific basis,
    Intergovernmental panel on climate change, 2001.

785 Randerson, J. T., Lindsay, K., Munoz, E., Fu, W., Moore, J. K., Hoffman, F. M., Mahowald, N. M., and Doney, S. C.:
    Multicentury changes in ocean and land contributions to the climate-carbon feedback, Global Biogeochemical Cycles,
    29, 744-759, https://doi.org/10.1002/2014GB005079, 2015.

Roberts, M. J., Jackson, L. C., Roberts, C. D., Meccia, V., Docquier, D., Koenigk, T., Ortega, P., Moreno-Chamarro, E.,
    Bellucci, A., and Coward, A.: Sensitivity of the Atlantic meridional overturning circulation to model resolution in
790   CMIP6 HighResMIP simulations and implications for future changes, Journal of Advances in Modeling Earth
    Systems, 12, e2019MS002014, 2020.

Rodgers, K. B., Sarmiento, J. L., Aumont, O., Crevoisier, C., de Boyer Montégut, C., and Metzl, N.: A wintertime uptake
    window for anthropogenic CO2 in the North Pacific, Global Biogeochemical Cycles, 22, 2008.

Rodgers, K. B., Aumont, O., Toyama, K., Resplandy, L., Ishii, M., Nakano, T., Sasano, D., Bianchi, D., and Yamaguchi, R.:
795   Low-latitude mesopelagic nutrient recycling controls productivity and export, Nature, 632, 802-807, 10.1038/s41586-
    024-07779-1, 2024.

Rodgers, K. B., Lee, S. S., Rosenbloom, N., Timmermann, A., Danabasoglu, G., Deser, C., Edwards, J., Kim, J. E., Simpson,
    I. R., Stein, K., Stuecker, M. F., Yamaguchi, R., Bódai, T., Chung, E. S., Huang, L., Kim, W. M., Lamarque, J. F.,
    Lombardozzi, D. L., Wieder, W. R., and Yeager, S. G.: Ubiquity of human-induced changes in climate variability,
800   Earth Syst. Dynam., 12, 1393-1411, 10.5194/esd-12-1393-2021, 2021.

Rodgers, K. B., Schwinger, J., Fassbender, A. J., Landschützer, P., Yamaguchi, R., Frenzel, H., Stein, K., Müller, J. D., Goris,
    N., Sharma, S., Bushinsky, S., Chau, T.-T.-T., Gehlen, M., Gallego, M. A., Gloege, L., Gregor, L., Gruber, N., Hauck,
    J., Iida, Y., Ishii, M., Keppler, L., Kim, J.-E., Schlunegger, S., Tjiputra, J., Toyama, K., Vaittinada Ayar, P., and Velo,
    A.: Seasonal Variability of the Surface Ocean Carbon Cycle: A Synthesis, Global Biogeochemical Cycles, 37,
805   e2023GB007798, https://doi.org/10.1029/2023GB007798, 2023.

Santer, B. D., Solomon, S., Pallotta, G., Mears, C., Po-Chedley, S., Fu, Q., Wentz, F., Zou, C.-Z., Painter, J., Cvijanovic, I.,
    and Bonfils, C.: Comparing Tropospheric Warming in Climate Models and Satellite Data, Journal of Climate, 30,
    373-392, https://doi.org/10.1175/JCLI-D-16-0333.1, 2017.

Sarmiento, J. L., Gruber, N., Brzezinski, M., and Dunne, J.: High-latitude controls of thermocline nutrients and low latitude
810   biological productivity, Nature, 427, 56-60, 2004.

Schuur, E. A. G., McGuire, A. D., Schädel, C., Grosse, G., Harden, J. W., Hayes, D. J., Hugelius, G., Koven, C. D., Kuhry,
    P., Lawrence, D. M., Natali, S. M., Olefeldt, D., Romanovsky, V. E., Schaefer, K., Turetsky, M. R., Treat, C. C., and
    Vonk, J. E.: Climate change and the permafrost carbon feedback, Nature, 520, 171-179, 10.1038/nature14338, 2015.

Screen, J. A., Deser, C., Smith, D. M., Zhang, X., Blackport, R., Kushner, P. J., Oudar, T., McCusker, K. E., and Sun, L.:
815   Consistency and discrepancy in the atmospheric response to Arctic sea-ice loss across climate models, Nature
    Geoscience, 11, 155-163, 2018.

Silva Dias, M. A. F., Dias, J., Carvalho, L. M. V., Freitas, E. D., and Silva Dias, P. L.: Changes in extreme daily rainfall for
    São Paulo, Brazil, Climatic Change, 116, 705-722, 10.1007/s10584-012-0504-7, 2013.

Smith, R., Jones, P., Briegleb, B., Bryan, F., Danabasoglu, G., Dennis, J., Dukowicz, J., Eden, C., Fox-Kemper, B., and Gent,
820   P.: The parallel ocean program (POP) reference manual ocean component of the community climate system model
    (CCSM) and community earth system model (CESM), LAUR-01853, 141, 1-140, 2010.

Sun, S., Shi, P., Zhang, Q., Wang, J. a., Wu, J., and Chen, D.: Evolution of future precipitation extremes: Viewpoint of climate
    change classification, International Journal of Climatology, 42, 1220-1230, https://doi.org/10.1002/joc.7298, 2022.

Tanioka, T., Garcia, C. A., Larkin, A. A., Garcia, N. S., Fagan, A. J., and Martiny, A. C.: Global patterns and predictors of C:
825   N: P in marine ecosystems, Communications earth & environment, 3, 271, 2022.

UN-DESA: World urbanization prospects, The 2018 Revison, 2018.

Vecchi, G. A. and Soden, B. J.: Global Warming and the Weakening of the Tropical Circulation, Journal of Climate, 20, 4316-
    4340, https://doi.org/10.1175/JCLI4258.1, 2007.

Vellinga, M. and Wood, R. A.: Global climatic impacts of a collapse of the Atlantic thermohaline circulation, Climatic change,
830   54, 251-267, 2002.

Waliser, D., Sperber, K., Hendon, H., Kim, D., Maloney, E., Wheeler, M., Weickmann, K., Zhang, C., Donner, L., and Gottschalck, J.: MJO simulation diagnostics, Journal of Climate, 22, 3006-3030, 2009.

Wang, G., Cai, W., and Santoso, A.: Variability of the Indian Ocean Dipole post-2100 reverses to a reduction despite persistent global warming, Nature Communications, 15, 5023, 10.1038/s41467-024-49401-y, 2024.

835 Weijer, W., Cheng, W., Garuba, O. A., Hu, A., and Nadiga, B. T.: CMIP6 Models Predict Significant 21st Century Decline of the Atlantic Meridional Overturning Circulation, Geophysical Research Letters, 47, e2019GL086075, https://doi.org/10.1029/2019GL086075, 2020.

Wheeler, M. and Kiladis, G. N.: Convectively coupled equatorial waves: Analysis of clouds and temperature in the wavenumber–frequency domain, Journal of the Atmospheric Sciences, 56, 374-399, 1999.

840 Zhang, L. and Karnauskas, K. B.: The role of tropical interbasin SST gradients in forcing Walker circulation trends, Journal of Climate, 30, 499-508, 2017.